A mutant with bilateral whisker to barrel inputs unveils somatosensory mapping rules in the cerebral cortex

Nicolas M Renier, Chloé M Dominici, Reha M Erzurumlu, Claudius F. Kratochwil, Filippo M Rijli, Patricia M Gaspar, Alain M Chédotal

A mutant with bilateral whisker to barrel inputs unveils somatosensory mapping rules in the cerebral cortex.

Nicolas Renier[1,‡,†], Chloé Dominici[1], Reha S. Erzurumlu[2], Claudius F. Kratochwil[3,#], Filippo M. Rijli[3,4], Patricia Gaspar[5] & Alain Chédotal[1, †]

1 Sorbonne Universités, UPMC Univ Paris 06, INSERM, CNRS, Institut de la Vision, 17 Rue Moreau, 75012 Paris, France.

2 Department of Anatomy and Neurobiology, University of Maryland School of Medicine, Baltimore, MD 21201-1075, USA

3 Friedrich Miescher Institute for Biomedical Research, CH-4058 Basel, Switzerland

4 University of Basel, 4003 Basel, Switzerland

5 INSERM, U839, Institut du Fer à Moulin, Paris, F-75005, France

‡ Present address : ICM – Brain and Spine Institute, Hôpital de la Pitié-Salpétrière, 47 Bd de l'Hôpital, 75013 Paris, France

Present address : Chair in Zoology and Evolutionary Biology, Department of Biology, University of Konstanz, Konstanz, Germany

†Correspondence should be addressed to Alain Chédotal, E-mail: alain.chedotal@inserm.fr, or Nicolas Renier, Email: nicolas.renier@icm-institute.org

Abstract

In mammals, tactile information is mapped topographically onto the contralateral side of the brain in the primary somatosensory cortex (S1). Here we describe that in Robo3 mouse mutants a sizeable fraction of the trigemino-thalamic inputs project ipsilaterally rather than contralaterally. The resulting mixture of crossed and uncrossed sensory inputs creates bilateral whisker maps in the thalamus and cortex. Surprisingly, these maps are segregated resulting in a duplication of whisker representations and a doubling of the number of barrels without changes of the S1 size. Sensory deprivation shows competitive interactions between the ipsi/contralateral whisker maps. This study reveals that the somatosensory system can form a somatotopic map to integrate bilateral sensory inputs but organizes the maps in a different way than in the visual, or auditory systems. Therefore, while the molecular pre-patterning constrains their orientation and position, the preservation of the continuity of inputs defines the layout of the somatosensory maps

Introduction

Sensory maps in the brain need to integrate physical (topographic) and functional constraints. According to the type of sensory modality, these constraints are differently accommodated. In the somatosensory system, the sensory receptors of the periphery establish topographic replicas in the different brain relay stations, in brainstem, thalamus and cortex, with a size that is roughly proportional to functional importance of the sensory element represented (Penfield and Boldrey, 1937; Woolsey and Van der Loos, 1970).

While some of the main construction principles of these maps have been elucidated implying a collaboration of morphogenetic gradients and neural activity (Fukuchi-Shimogori and Grove, 2003; Pfeiffenberger et al., 2005; Rash and Grove, 2006), a point of continued controversy is the degree to which the initial clustering and topographical arrangement of axons carrying the inputs plays a role in map layout (Erzurumlu and Gaspar, 2012).

The contributions of molecular pre-patterning versus nearest-neighbor clustering can be tested in bilateral sensory maps that integrate bilateral signals where the inputs come from each side of the body and therefore arrive via separate routes. Manipulating the laterality of inputs can also be a way to probe the mechanisms of bilateral integration during map-building. This has been tested previously in the visual system (Rebsam et al., 2009). However, the natural overlap of the receptive fields for a portion of retinal ganglion cells between the left and right eyes could also constrain the topographic organization of the binocular visual cortex. Thus experiments done in the visual system do not allow easy disambiguation of the different mechanisms at play during the establishment of the map. Evidently, there is no such continuity and

overlap between the somatosensory receptive fields of the left and right sides of the body. Therefore, if genetic patterning were the main factor controlling the integration of bilateral sensory processing in the cortex, one would expect that changing the laterality of a fraction of somatosensory inputs would create an equivalent of a "binocular" region in the somatosensory cortex. To the opposite, if the map-building rules maintains nearest-neighbor's interactions, one would expect that such manipulation would result in a fully segregated representation of bilateral inputs in the cortex. Here we examined the effect of partial uncrossing of presynaptic afferents to the somatosensory thalamus in the whisker to barrel pathway of mice.

The sensory afferents from the whisker follicles first synapse in the brainstem trigeminal complex and second order neurons in the principal sensory nucleus of the trigeminal nerve (PrV) carry the whisker-specific inputs to the contralateral ventroposteromedial nucleus (VPM) of the thalamus (**Figure 1A**; reviewed in (Erzurumlu et al., 2010)). In the present study we focused on a conditional mouse mutant in which *Robo3*, an axon guidance receptor necessary for the crossing of commissural axons (Sabatier et al., 2004) is inactivated in rhombomere 3 (Renier et al., 2010), the origin of most whisker-specific PrV neurons (Oury et al., 2006). The conditional lack of Robo3 only caused a partial crossing defect of trigemino-thalamic axons. Consequently, conditional Robo3 mutants had bilateral sensory afferents in the brainstem to neocortex portion of the whisker-barrel pathway. We found that this resulted in the appearance of two functional whisker maps in the thalamic relay, VPM, and the barrel cortex, each receiving inputs from a different side of the animal's face. Most interestingly, these maps were entirely segregated, both being confined to the cortical space normally allocated to the facial whisker representation, retaining a correct orientation, and topographic organization. These results suggest that the

mechanisms shaping the topographic representation of the somatosensory map respect the nearest-neighbor continuity of the peripheral receptors topography, within the position and orientation constrains set by the molecular pre-patterning gradients in the thalamus and cortex.

Results

Genetic perturbation of midline crossing signals and emergence of bilateral somatosensory maps.

We analyzed the whisker to barrel projection in a previously characterized mouse line (Renier et al., 2010) in which the *Robo3* gene has been specifically knocked out in rhombomeres 3 (r3) and r5, using the Krox20 promoter (*Krox20:Cre;Robo3*$^{lox/lox}$, named *Robo3*$^{R3\text{-}5}$*-cKO* thereafter, while *Krox20:Cre;Robo3*$^{lox/+}$ are named *Robo3*$^{R3\text{-}5}$*-Het*). During development, *Robo3* is transiently expressed in r3 neurons, with an expression that stops shortly after axon crossing, suggesting that it does not play a role in later stages of development such as axon targeting (Badura et al., 2013; Michalski et al., 2013; Renier et al., 2010). As expected, *in situ* hybridization confirmed that *Robo3* expression is deleted from r3 in 12 days old (E12) *Robo3*$^{R3\text{-}5}$*-cKO* embryos (**Figure 1B**, n= 3/3).

To visualize the trigemino-thalamic pathway, we crossed *Robo3*$^{R3\text{-}5}$*-cKO* mice to *Tau-lox-Stop-lox-mGFP-IRES-nls-lacZ* mice (*Tau*^{GFP}) (Hippenmeyer et al., 2005). In E12 controls many GFP+ axons cross the midline at the r3 and r5 level (**Figure 1B-D)**. The ßGal nuclear reporter showed a dense distribution of Krox20+ cell bodies in the ventral region of the PrV nucleus as expected from previous fate-mapping experiments (Oury et al., 2006). In the *Robo3*$^{R3\text{-}5}$*-cKO;Tau*^{GFP}, the distribution of ßgal+ neurons, and organization of barrelettes was normal, indicating that ROBO3

deletion did not alter the development of the PrV nucleus (**Figure 1C and Figure 1-figure supplement 1**). By contrast, most of the GFP-labelled axons arising from the PrV failed to cross, although they still projected rostrally towards the forebrain (**Figure 1B-D**; n=3/3). At E13, coronal sections at the level of r3 showed that the density of GFP+ commissural axons at the ventral midline was strongly reduced in the *Robo3$^{R3\text{-}5}$-cKO;Tau^{GFP}* but also indicated that a subset of axons still crosses (**Figure 1B**). Double staining for NeuN and the nuclear cre reporter ß-gal in adult sections of *Robo3$^{R3\text{-}5}$-Het;Tau^{GFP}* mice (**Figure 1-figure supplement 1;** n=5) showed that 88% NeuN+ neurons in the ventral part of PrV express ßgal but that a small subset of the NeuN+ PrV neurons (10.7± 1.5%) was not ßgal+ and probably did not express Cre recombinase.

As ephrins and their receptors have been shown to control the targeting and orientation of thalamocortical projections for visual or somatosensory axons (Dufour et al., 2003; Pfeiffenberger et al., 2005), we checked the pattern of *ephrin-A5* mRNA expression at P0 in controls and *Robo3$^{R3\text{-}5}$-cKO* mutants by in-situ hybridization. The expression gradients of *ephrin-A5* in the cortex and thalamus were not noticeably different in the mutants compared to controls (**Figure 1E**, (n=2)) suggesting that the deletion of Robo3 in the brainstem did not affect the expression of patterning cues in the thalamus and cortex.

3D imaging of the trajectory of the trigemino-thalamic (TT) tract from the brainstem to the thalamus using iDISCO (Renier et al., 2014) (**Figure 2A**) revealed that at P4, the GFP+ axons had a similar trajectory in the TT tract in both the control and mutant mice (n=5), although the tract appeared slightly more defasciculated in the mutants. GFP+ axon terminals arborized in the VPM in both control and mutant mice and formed barreloids (**Figure 2A, B; Video 1**). In all mutants and controls (n=14 for each

genotype), the r3-derived GFP+ (r3-GFP+) axons projected to the dorsolateral VPM containing the barreloids (**Figure 2B**). An abnormal organization of the whisker barreloids was noted in the mutant VPM. In controls, all the barreloid rows coincided with a dense r3-GFP+ axon territory (**Figure 2B**; n=4/4), whereas in mutants two distinct zones were observed (n=4/4): a lateral VPM domain containing a high density of GFP+ axons and a medial VPM domain with only sparse patches of GFP+ axons (**Figure 2B**). These two VPM domains contained barreloids as noted with cytochrome oxidase staining and were of comparable surface area in coronal sections through the middle of the VPM (0.19±0.006 mm^2 for the lateral dense GFP+ domain and 0.18±0.003 mm^2 for the medial patches of GFP+ domain, P=0.46). Moreover, they were separated by a cytochrome oxidase-free septum. These observations suggested that in the *Robo3*$^{R3\text{-}5}$*-cKO* mice, the VPM became split into two separate domains, each with a different barreloid patterning (although the lateral one contains the highest density of the r3-derived projections, and the larger barreloids).

We anterogradely traced the PrV to VPM projections in P4 *Robo3*$^{R3\text{-}5}$*-cKO* mice using carbocyanine dyes. In control mice the PrV-VPM projection was completely crossed whereas in mutants the VPM received a bilateral innervation from the PrV (**Figure 2C**). Moreover, the position, shape and size of the traced projections in the VPM was reminiscent of the two domains described previously, suggesting that in the mutants, the dense GFP+ lateral region might correspond to abnormal ipsilateral projections from the PrV, while the medial patches might be originating from the contralateral side.

These observations indicate that the mutant VPM receives segregated ipsilateral and contralateral trigemino-thalamic inputs. Retrograde injections from the VPM labeled

cell bodies on both contralateral and ipsilateral trigeminal PrV nuclei in *Robo3*$^{R3\text{-}5}$-*cKO* mutants (3.3 times (n=3) more cell bodies were labeled ipsilaterally than contralaterally) (**Figure 2D**; n=4/4). Interestingly, the neurons projecting ipsilaterally and contralaterally were mixed in the ventral PrV in the *Robo3*$^{R3\text{-}5}$*-cKO* mutants, in contrast with the segregation of their projections seen with the anterograde tracings. Overall these data suggest that a large fraction of the rhombomere 3-derived trigemino-thalamic axons project ipsilaterally in *Robo3*$^{R3\text{-}5}$*-cKO* mutants but that some still project contralaterally either because Cre recombination was incomplete or occurred after crossing.

It is possible that the timing of arrival of the ascending axons in the VPM could participate in the segregation of the ipsilateral and contralateral domains because of their shorter path in the mutants. Ipsilateral axons in mutants may reach the VPM first and occupy the dorso-lateral quadrant of the VPM normally populated by the larger barreloids in controls. We looked at the development of the trigemino-thalamic (TT) tract at E15.5 in *Robo3*$^{R3\text{-}5}$*-cKO;Tau*^{GFP} mutant embryos, when axons from the PrV have not yet reached their targets in the VPM (**Figure 2-figure supplement 1A**, n=3) (Kivrak and Erzurumlu, 2013). In this line, both ipsilateral and contralateral PrV projections to the VPM are GFP+. To selectively label contralateral PrV axons, we injected DiI unilaterally into the PrV. In the TT tract, red axons (DiI+ only), yellow axons (double positive for GFP and DiI), and green axons (GFP+) were organized in a medial to lateral gradient (**Figure 2-figure supplement 1A**, n=3), suggesting that ipsilateral and contralateral axons in the TT tract might be pre-sorted before reaching their target. Ipsilateral (green only) axons were always seen next to contralateral axons (red and yellow) in the TT tract up to the rostral-most sections containing the endings/growth cones of the developing axons. Therefore, ipsilateral axons had no

measurable lead over contralateral axons before reaching the VPM at this stage. Indeed, in both *Robo3*$^{R3\text{-}5}$*-Het;Tau*^{GFP} and *Robo3*$^{R3\text{-}5}$*-cKO;Tau*^{GFP} mutants E18 embryos, the TT have reached the VPM and its terminals fill the whole dorsal region (Kivrak and Erzurumlu, 2013) (**Figure 2-figure supplement 1B**, n=3). However, the precise timing of arrival for the contralateral and ipsilateral axons in the mutant VPM is difficult to assess. While we did not find evidence for a delayed arrival of the contralateral TT projections in the VPM, we cannot rule out that ipsilateral projections reach their targets earlier and hence have a competitive advantage to innervate the VPM.

To determine the 3D organization of the VPM map in the *Robo3*$^{R3\text{-}5}$*-cKO* mutants, and the origin of the GFP+ patches, we performed whole-mount imaging of brains from *Robo3*$^{R3\text{-}5}$*-cKO;Tau*^{GFP} mutants and heterozygous controls at P8 using iDISCO (**Figure 3**)(Belle et al., 2014; Renier et al., 2014). A suitable angle was determined for the optimal projection of the barreloids in the thalamic whisker map onto a plane: 3D datasets where oriented at a 45° oblique angle from both coronal and horizontal planes (**Figure 3A, Figure 3-figure supplement 1A and Video 2**). In the *Robo3*$^{R3\text{-}5}$*-cKO;Tau*^{GFP} mutants, the GFP dense and patched regions were manually segmented to show their respective 3D domains. In both regions, barreloids were organized in rows reminiscent of the control VPM map (**Figure 3A and Figure 3-figure supplement 1B**, n=3).

To determine whether each region corresponded to a distinct whisker map we performed unilateral lesions of the infraorbital nerve (ION) at P0 and the GFP+ projections in the VPM were imaged at P8. In control mice, the unilateral ION lesions caused a fusion of the barreloids in the contralateral VPM (**Figure 3B and Figure 3-figure supplement 1C**; n=3**).** In mutants barreloid-fusion was found in both the

ipsilateral and the contralateral VPM: ipsilaterally, in the GFP-dense region, and contralaterally in the GFP-patched region (**Figure 3B**, n=5). This indicated that, as suggested by the tracing experiments, the GFP dense region in the VPM receives ipsilateral inputs from the PrV, whereas the GFP-patched region receives contralateral inputs. This also demonstrated that the GFP-patched region carries somatosensory inputs from the infraorbital branch of the trigeminal nerve. Moreover, in addition to the fusion of the barreloids, the thalamic map that sustained sensory deprivation was reduced in size, while the adjacent non-deprived map was enlarged (**Figure 3C**, n=5). This showed that sensory-activity-based competition defines the final space allocated to each map in the mutant VPM.

To verify whether both maps in the VPM received inputs from the periphery, we performed an intact brain c-Fos immunolabeling in control and mutant mice whose whiskers were shaved on the left side, and b, d rows were spared on the right side (n=3). The intact brain immunolabeling gave us the opportunity to navigate the complex 3D organization of the VPM using arbitrary oblique projection planes (**Figure 4A**). In controls, two bands of c-Fos+ cells were seen contralateral to the spared whiskers, revealing the B and D rows barreloids (**Figure 4B**). In *Robo3*$^{R3\text{-}5}$*-cKO* mice, a dual band pattern in the VPM was seen on both sides of the brain. In the ipsilateral VPM, the bands were visible on the same intersecting plane as controls. On the contralateral VPM, the bands of activity were visible on a a more medial plane, at the edge of the VPM annotation.

Overall these experiments provide a model for the organization of the VPM in *Robo3*$^{R3\text{-}5}$*-cKO* mutant mice (**Figure 3D** and **Figure 4C**). In the mutant VPM, sensory inputs from the ipsilateral PrV establish a dorsolateral map, with dense projections. Adjacent to this map, inputs from the contralateral PrV project to the dorso-medial

VPM as discrete patches. These 2 thalamic maps are organized in rows, reminiscent of the normal thalamic map. Our finding that whisker stimulation triggers activity-related expression in the 2 VPM maps in the mutant suggests that the barreloid organization is functional (**Figure 4C**).

Formation of bifacial cortical maps

Next, we determined how the VPM organization in the mutant influences the formation of the somatosensory map in the cerebral cortex. Tangential sections through layer 4 were stained for cytochrome oxidase and Vglut2 immunoreactivity to label thalamocortical afferents (Nahmani and Erisir, 2005) (**Figure 5A and Figure 5-figure supplement 1A**). A striking abnormality in the layout of thalamic afferents was noted in the posteromedial barrel subfield (PMBSF, which corresponds to the representation of the large whiskers) of S1 in *Robo3*$^{R3\text{-}5}$*-cKO* mice (n=5/5; **Figure 5A**). Large barrels were extra-numerous (52±2 barrels in mutant PMBSF *vs.* 33±0 in controls), and were reduced in size (0.04mm^2 ± 0.01 per barrel in mutants, compared to 0.09mm^2±0.02 in controls, P<0.0001). Moreover, they were arranged into 8 rather than the usual 5 whisker rows, with a clear delineation of two separate cortical zones, a central zone, and a peripheral zone, each containing distinct barrel rows (**Figure 5A and Figure 5-figure supplement 1-3**). These abnormalities were similar in both hemispheres and at all ages analyzed (with only slight individual variations; n=25/25; **Figure 5-figure supplement 1-3**). To map the functional whisker representation in this unusual map, we monitored the activation of the immediate early gene c-Fos following a one-hour exposure to an enriched sensory environment (Staiger et al., 2000). In mice with unilateral trimming of the whiskers (**Figure 5B**) strong c-Fos labeling is normally observed only in the S1 contralateral to the intact whiskers. In

Robo3$^{R3\text{-}5}$*-cKO* mice with unilateral whisker trimming, c-Fos was activated in the PMBSF of both hemispheres (**Figure 5B**). Contralateral to the intact whiskers, c-Fos activation was visible in the peripheral barrel rows (contra domain; **Figure 5B**). Ipsilateral to the intact whiskers, a mirror image was noted with c-Fos activation in the central barrel rows (Ipsi domain; **Figure 5B**). In both contralateral and ipsilateral patterns, c-Fos+ cells were detected in all layers from the columns of the stimulated barrels (**Figure 5B-figure supplement 3B**). These results showed that in *Robo3*$^{R3\text{-}5}$*-cKO* mice, the crossed and uncrossed trigemino-thalamic inputs are mapped as two segregated domains, the ipsilateral one nested within the contralateral map (**Figure 5B**).

Orientation and polarity of the maps.

The segregation of the two maps led to the question of its topographic organization. Two scenarios are possible: i) the thalamic afferents follow topographic molecular guidance cues expressed in the cortex, with complementary receptor expression in the thalamus; in this case one would expect that neighboring whiskers of the ipsi- and contralateral map lie in register with one another; ii) the thalamic afferents are clustered following sensory activity-based rules leading functionally coordinated afferents to cluster together; in this scenario, the topographical rule of near neighbors would prevail over molecular gradients.To analyze the topographic alignment of the crossed and uncrossed somatosensory maps we monitored c-Fos expression in S1 after clipping all whiskers except one row or one arc of whiskers on one side (**Figure 5C** and data not shown). When the 5 posterior most whiskers of the whisker pad (A1-E1; **Figure 5C**) were left intact in control mice, this resulted in the activation of c-Fos in a caudal arc of 5 barrels exclusively in the contralateral S1 (**Figure 5C**). Likewise,

when the second whisker row (B1-B4; **Figure 5C**) was left intact, the corresponding row of barrels was activated in the contralateral S1 (**Figure 5C**). In mutants, c-Fos activation was bilateral, with a labeling in both the central (ipsi) and peripheral (contra) PMBSF domains (**Figure 5C**). The general orientation of the two nested maps was similar and resembled that of control mice likely due to the patterning activity of morphogens that determine the polarity of the map (Fukuchi-Shimogori and Grove, 2001; 2003). However, unlike the visual or auditory bilateral maps, we observed that there were discontinuities in the organization of the bilateral somatotopic map, such as a lack of topographic proximity of the ipsi/contra representation for a given barrel or barrel row. Rather, there appeared to be a clear separation and independence of the ipsi- and contralateral inputs. Taken together, these results favor the hypothesis that nearest-neighbor's interactions prevail to some extent over the molecular pre-patterning to organize a continuous representation of the periphery for each map. However, the molecular gradients still contribute to maintain the general orientation of the maps.

Competition between ipsi- and contralateral inputs for cortical space

The space occupied by the barrel map was not increased in mutants (2.32±0.05 mm^2 in controls *vs* 1.90±0.12 mm^2 in mutants, P=0.04) unlike in other mouse models with duplication of the S1 map where a second S1 map is formed at the expense of other cortical areas (Fukuchi-Shimogori and Grove, 2001; 2003). This suggested that the ipsi- and contralateral thalamic inputs compete to occupy a defined cortical space in S1. Accordingly, individual barrels in mutants were roughly half the size (44± 2%) of controls. As with the VPM, we looked again at the consequences of unilateral deprivation of whisker inputs induced by a neonatal (P1) lesion of the ION (Waite and

Cragg, 1982). In control mice, barrel-fusion was observed in the S1 contralateral to the lesion (**Figure 6A**; n=3/3). In mutants, barrels fused in the maps corresponding to the ipsi- and contralateral representations of the lesioned whisker pad (**Figure 6A**; n=5/5). Furthermore, the representation of the unlesioned side expanded at the expense of the fused-map. This suggests that there is a sensory activity-dependent competition for cortical space between the ipsilateral and contralateral sensory inputs in the mutant S1.

Finally, we checked whether the ipsilateral and contralateral maps were functionally isolated. We took advantage of the ClearMap pipeline (Renier et al., 2016) to compare c-Fos activity patterns in the whole brain in an unbiased way , in the unilateral whisker stimulation protocol (n=3 per group) (**Figure 7A and Figure 7-figure supplement 1**). We looked for brain regions that exhibited left-right differences that were opposite in controls and mutants. As expected, the barrel cortex and VPM exhibited statistically significant differences between the shaved and stimulated sides of the brain, that were opposite between controls and mutants (**Figure 7A**). Of note, the column of activity detected in d-row registered precisely in the same position in control and mutants, showing that the absolute position of the d row in the brain is the same in the aberrant ipsilateral map of the mutant mice than in controls. We then isolated c-Fos+ cells from the upper cortical layers (n=4). In upper layers, contrary to layer 4, activity patterns are not restricted to the stimulated barrels (**Figure 7B**), but expand over adjacent barrels, due to downstream cortical integration (Kaliszewska et al., 2012; Peron et al., 2015). We looked at the effect of a patterned sensory deprivation created by trimming rows b and d on one side and shaving all whiskers on the other side. Expansion of c-Fos+ cells was observed

within both maps between activated rows in the upper cortical layers 2-3 (**Figure 7B**), but not across the boundaries of each map. This suggests that the ipsilateral and contralateral whisker maps have little to no direct horizontal integration in the upper cortical layers.

Discussion

Here we show that uncrossing a sizeable fraction of the trigemino-thalamic axon tracts results in an unexpected anatomical and functional organization in the thalamus and neocortex: a duplication of the facial whisker representation with two segregated maps sharing the same cortical space allotted to somatosensory function. If the targeting of the ascending axons was solely organized in a point-to-point manner by patterning gradients in the thalamus and cortex, this genetic manipulation should have resulted in the formation of an interspersed “biwhisker” representation of the whiskers in both thalamic and cortical relays. Instead, we observed a complete segregation of the ipsi and contralateral whisker maps, each map following the spatial continuity of inputs from the whiskers. However each map retained a correct orientation and topographic organization. This shows that genetic pre-patterning and the preservation of the continuity of inputs interact to control respectively the position and layout of the somatosensory maps. The absence of left-right mixing of inputs in the *Robo3*$^{R3\text{-}5}$*-cKO* mutant somatosensory cortex also suggests that the mechanisms allowing the integration of bilateral inputs in the visual cortex might be absent in the somatosensory cortex.

The effect of uncrossing commissures has been studied in the same conditional Robo3 mutant in other systems: the olivo-cerebellar projections (Badura et al., 2013)

and the auditory projections from the cochlear nucleus to the medium nucleus of the trapezoid body (Michalski et al., 2013). In these two studies, it was found that affecting the laterality of the projections did not affect the topographic targeting of the uncrossed axons. However, in the case of the calyx of Held, the maturation of the uncrossed synapses was delayed (Michalski et al., 2013). It is unclear whether midline crossing changes the molecular expression profile of the axons to promote the synaptic maturation or whether this is an indirect effect of an incorrect integration within an otherwise normal network. It would be important to check the physiological properties of the ipsilateral map, especially because this new model provides the opportunity to study the cortical integration of an abnormal circuit.

The absence of bilateral integration between the two maps in the cortex of *Robo3* mutants strikingly differs from what is observed in the binocular region of the visual cortex (Sato and Stryker, 2008). The particular organization of the two embedded whisker maps emphasizes an important characteristic of the somatosensory system which combines two different mapping rules, the first being the continuous topographic representation of the body surface, the second being an organization into distinct functional units. The organization of bilaterality in the somatosensory cortex happens differently when forced in the *Robo3*$^{R3\text{-}5}$*-cKO mice* than in the normal visual cortex. This raises the tantalizing possibility that specific molecular and activity-based mechanisms absent from the somatosensory system have appeared in the visual system to promote the integration of bilateral information in the cortex, and could therefore be an evolutionary mechanism governing how sensory information is processed in *Bilateria*.

Orientation of representations and cortical plasticity

Contrary to previous observations of experimental map duplication (Fukuchi-Shimogori and Grove, 2001) the present orientation of the two whisker maps was similar in the general rostrocaudal and mediolateral axes, indicating that matching gradients of guidance molecules and their receptors was most likely unchanged, which was confirmed for ephrin-A5 (**Figure 1E**). This contrasts with the mirror image organization of the sensory maps obtained when inducing novel sources of molecular gradients in the somatosensory cortex (Fukuchi-Shimogori and Grove, 2001). This also contrasts with observations of map duplication in the visual system, caused by a change in the retinal axon crossing at the midline (Petros et al., 2008; Rebsam et al., 2009), by lack of one eye (Trevelyan et al., 2007) or by lack of one hemisphere (Muckli et al., 2009).

The normal orientation of the ipsilateral map in the mutants is surprising. One might have expected that switching laterality of the normally crossed projections would flip the axis of the ipsilateral map from the contralateral map to account for the chiral organization of the left and right sides of the face. As both maps in the mutants respect the normal orientation, the ascending tract from the ipsilateral side may either undergo a torsion en route to the VPM to correct the orientation based on molecular gradients present in the lemniscal pathway. Alternatively, the correction of the orientation may occur only at the target site in the VPM based on the gradients of expression of Eph receptors/ephrin ligands in a process akin to the visual tectum (Feldheim et al., 1998; Tessier-Lavigne, 1995). If true, this hypothesis implicates the presence of additional mechanisms of axonal pruning and refinement as seen during the post-targeting development of visual projections (Nakamura and O'Leary, 1989; Simon et al., 2012) to correct the final orientation of the ipsilateral map.

In conclusion, although the initial wiring of the brain largely relies on genetically encoded processes, our results further illustrate the remarkable plasticity of the mammalian brain and its ability to accommodate changes in afferent wiring in evolution to create new maps and bilateral representations, and also its ability, in the context of developmental brain disorders, to compensate for major axon guidance defects that otherwise would lead to severe brain dysfunction (Jen et al., 2004; Muckli et al., 2009; Williams et al., 1994).

Materials and Methods

Mice

All animal procedures were carried out in accordance to institutional guidelines (UPMC, Charles Darwin ethic committe and INSERM). Mice were anesthetized with Ketamine (Virbac) and Xylazine (Rompun). The day of vaginal plug is embryonic day 0 (E0) and the day of birth corresponds to postnatal day 0 (P0).

The Robo3 conditional knockout, *Krox20:Cre* knock-in and *Tau*^{GFP} lines were previously described (Hippenmeyer et al., 2005; Renier et al., 2010; Voiculescu et al., 2000). Unless otherwise mentioned, controls were *Robo3*$^{lox/lox}$ or *Krox20:Cre;Robo3*$^{lox/+}$ animals. Double heterozygotes were always similar to wild-type mice. Mice were genotyped by PCR.

The following primers were used for genotyping: the conditional *Robo3* allele, 5'-CCA AGG AAA AAC TTG AGG TTG CAG CTA G-3' and 5'-GAT TAG GGG AGG TGA GAC ATA GGG-3', the *Krox20:Cre* allele, 5'-AGT CCA TAT ATG GGC AGC GAC-3' and 5'-ATC AGT GCG TTC GAA CGC TA-3', the T*au*^{GFP} allele, 5'-GAG GGC GAT GCC ACC TAC GGC AAG-3' and 5'-CTC AGG GCG GAC TGG GTG CTC AGG-3'. All PCR run have 34 cycles with an annealing temperature of 58°C.

In the *Tau*^{GFP} line, upon Cre recombination in neurons, the Stop cassette is excised leading to the permanent expression of a myristoylated GFP in axons and of ß-galactosidase in nuclei (Hippenmeyer et al., 2005).

Histology and immunocytochemistry

Mice were perfused transcardially with a 4% PFA in 0.12 mM phosphate buffer. Cortices were flattened between microscope slides and post-fixed in 4% PFA and vibratome (Leica) sectioned at 50µm. Hindbrains and thalamus were post-fixed in 4% PFA, cryoprotected in 30% sucrose and sectioned at 35µm with a freezing microtome (Microm).

For cytochrome oxidase staining (Melzer et al., 1994), sections were incubated at room temperature for 24 hours in 10% sucrose, 0.3g/L cytochrome C from equine heart (Sigma), 0,02g/L catalase from bovine liver (Sigma) and 0.25g/L DAB (Sigma). The endogenous fluorescence of the GFP in *Krox20:Cre;Tau*^{GFP} was not affected after the treatment and could be imaged on the same sections, however the GFP signal was further enhanced by immunostaining.

For immunohistochemistry, neonatal and adult brains were processed as described previously (Marillat et al., 2002). The following primary antibodies were used: guinea pig anti-Vglut2 (1:1000, Millipore AB-2251), rabbit anti-βGal (1:1000, 55976 Cappel), rabbit anti-c-Fos (1:1000, sc-52 Santa-Cruz on sections, or 1:2000, 226-003 Synaptic Systems, for iDISCO+ studies), rabbit anti-GFP (1:300, A11122 Invitrogen on sections), chicken anti-GFP (1:800, ab13970 Abcam on sections or 1:2000, GFP-1020 Aves for iDISCO studies). The following secondary antibodies were used on sections: Donkey anti-mouse, anti-rabbit and anti-guinea pig coupled to CY3 or CY5 (1:600, Jackson Laboratories), donkey anti-mouse, anti-rabbit and anti-chicken

coupled to Alexa Fluor 488, 568 or 657 (1:600, Invitrogen) for sections and iDISCO studies. Sections counterstained with Hoechst 33258 (10 µg/mL, Sigma)

Sections were examined with a fluorescent microscope (DM6000, Leica) equipped with a CoolSnapHQ camera (Roper Scientific), a confocal microscope (FV1000, Olympus), or a slide scanner (Nanozoomer, Hamamatsu).

iDISCO+ processing and light sheet microscopy

Adult mice or P4, P8 pups were euthanized with a rising gradient of CO_2 and fixed with an intracardiac perfusion of 4% PFA in PBS. All harvested samples were post-fixed overnight at 4°C in 4% PFA in PBS.

Fixed samples were washed in PBS for 1h twice, then in 20% methanol (in ddH_2O) for 1h, 40% methanol for 1h, 60% methanol for 1h, 80% methanol for 1h, and 100% Methanol for 1h twice. Samples were then bleached with 5% H_2O_2 (1 volume of 30% H_2O_2 for 5 volumes of methanol, ice cold) at 4°C overnight. After bleaching, samples were re-equilibrated at room temperature slowly and re-hydrated in 80% methanol in H_2O for 1h, 60% methanol / H_2O for 1h, 40% methanol / H_2O for 1h, 20% methanol / H_2O for 1h, and finally in PBS / 0.2% TritonX-100 for 1h twice.

Pre-treated samples were then incubated in PBS / 0.2% TritonX-100 / 20% DMSO / 0.3M glycine at 37°C for 36h, then blocked in PBS / 0.2% TritonX-100 / 10% DMSO / 6% donkey serum at 37°C for 2 days. Samples were then incubated in primary antibodies: chicken anti-GFP (1:2000, Aves GFP-1020), rabbit anti-c-Fos (, 1:2000, Synaptic Systems, 226-003) in PBS-Tween 0.2% with heparin 10µg/mL (PTwH) / 5% DMSO / 3% donkey serum at 37°C for 4 to 7 days. Samples were then washed in PTwH for 24h (5 changes of the PTwH solution over that time), then incubated in secondary antibody donkey anti-rabbit-Alexa647 from Invitrogen or donkey anti-

chicken from Jackson Immunoresearch at 1:500 in PTwH / 3% donkey serum) at 37°C for 4 to 7 days. Samples were finally washed in PTwH for 1d before clearing and imaging. Immunolabeled brains were dehydrated in 20% methanol (in ddH_2O) for 1h, 40% methanol / H_2O for 1h, 60% methanol / H_2O for 1h, 80% methanol / H_2O for 1h, and 100% Methanol for 1h twice. Samples were incubated overnight in 1 volume of methanol / 2 volumes of dichloromethane (DCM, Sigma 270997-12X100ML) until they sank at the bottom of the vial (plastic Eppendorf tubes were used throughout the process). The methanol was then washed for 20min twice in 100% DCM. Finally, samples were incubated (without shaking) in DiBenzyl Ether (DBE, Sigma 108014-1KG) until clear (about 30min) and then stored in DBE at room temperature.

Cleared samples were imaged in sagittal orientation (right lateral side up) on a light-sheet microscope (Ultramicroscope II, LaVision Biotec) equipped with a sCMOS camera (Andor Neo) and a 2X/0.5 objective lens (MVPLAPO 2x) equipped with a 6mm working distance dipping cap. Version v144 of the Inspector Microscope controller software was used. The microscope is equipped with LED lasers (488nm and 640nm) with 3 fixed light sheet generating lenses. Scans were made at the 0.8X zoom magnification (1.6X effective magnification), with a light sheet numerical aperture of 0.1. Emission filters used are 525/50 and 680/30. The samples were scanned with a step-size of 3µm using the continuous light sheet scanning method with the included contrast blending algorithm for the 640nm channel (20 acquisitions per plane with a 50ms exposure), and without horizontal scanning for the 480nm channel (50ms exposure). To speed up the acquisitions, both channels where acquired in two separate scans.

Maximum 3D projections in **Figure 2A** and all panels of **Figure 3**, **4** and **7B** were performed using Imaris (Bitplane, http://www.bitplane.com/imaris/imaris), and

generated from manual 3D segmentation of the raw data using the surface tool. ClearMap (Renier et al., 2016) (https://www.idisco.info) was used to quantify and register c-Fos+ cells in **Figure 7A**. Parameters were set as previously described, and automated isolation of the cortex was done using the scripts available online.

In situ hybridization

Antisense riboprobes were labeled with digoxigenin-11-D-UTP (Roche Diagnostics) as described previously (Marillat et al., 2002) by in vitro transcription of mouse cDNAs encoding *robo3* or an exon specific probe of *robo3* targeting the floxed region (Renier et al., 2010).

DiI tracing

4% PFA fixed P4 pups were injected with small crystals of 1,1'-dioctadecyl-3,3,3',3'-tetramethylindocarbocyanine perchlorate (DiI, Invitrogen) and 4-(4-(dihexadecylamino)styryl)-*N*-methylpyridinium iodide (DiA, Invitrogen) using glass micropipettes. For anterograde tracing, the dye crystals were injected unilaterally in the PrV. For retrograde tracing of the PrV nuclei, the cortices were removed to expose the thalamus and DiI or DiA crystals were at the level of the VPM.

Brains were kept at 37°C for 4 weeks. Brains were cut in 80 µm sections with a vibratome (Leica) and counterstained with Hoechst.

Infraorbital nerve lesions

P0-P1 pups were cold anesthetized, and an incision was made between the whisker pad and the eye. The nerve was cut with scissors under a dissecting scope. The pups were allowed to recover for 10 days and then perfused.

539

540 *c-Fos expression and whisker activity*

541 P20-P30 mice were anesthetized with ketamine, and all whiskers were trimmed on
542 the left side. In different experiments, either all whiskers were spared on the right
543 side, or only selected whisker rows or arcs were spared. Mice were allowed to
544 recover from anesthesia for 6 to 12 hours, and then left alone in a large (1m x 60cm)
545 "enriched" cage in the dark for 1 hour before being perfused and processed for c-Fos
546 immunostaining.

547

548 *Quantifications and statistical analysis*

549 Areas were calculated with NDPview (Hamamatsu) from cytochrome oxidase
550 staining at P10 or Vglut2 stainings when done in adults. For quantification of map
551 areas from P10 flattened cortices, the surface in controls was limited to the first 4
552 barrels in row a, 4 in row b, 6 in row c, 7 in row d and 8 in row e. In
553 *Krox20:Cre;Robo3*$^{lox/lox}$ mutants, the central (ipsi) map area comprises the domain
554 bordered by a thick Vglut2-negative boundary. The peripheral (contra) map area was
555 limited to the barrels located immediately above and below the border of the central
556 ipsi map. To determine individual barrel areas in adults, only the largest
557 unambiguous barrels were measured (first 3 barrels for rows e,d,c and first barrels
558 for rows a and b). Areas where assessed on the tangential section showing the most
559 complete map of the PMBSF.

560 The areas of the VPM nucleus were calculated with NDPview from frontal sections of
561 P4 *Krox20:Cre;Tau*^{GFP} mice stained with cytochrome oxidase and immunostained for
562 GFP, at a mid-level of the VPM, where the barreloids organization was the most
563 obvious.

Results are presented as means ± SEM. Differences of the means between two sample sets were assessed by two-tailed non-parametric Mann-Whitney test. Statistics were carried out with Prism (Graphpad software).

Acknowledgements

We thank P. Charnay for providing the *Krox20:Cre* line, and S. Arber for the Tau^{GFP} mice. We also thank N. Narboux-Nême for technical help. FMR laboratory was supported by the Swiss National Science Foundation (31003A_149573) and the Novartis Research Foundation. The teams of AC and PG are part of the Ecole des Neurosciences de Paris training network.

Competing interests

We declare no competing interests

References

Badura, A., Schonewille, M., Voges, K., Galliano, E., Renier, N., Gao, Z., Witter, L., Hoebeek, F.E., Chédotal, A., and De Zeeuw, C.I. (2013). Climbing fiber input shapes reciprocity of Purkinje cell firing. Neuron *78*, 700–713.

Belle, M., Godefroy, D., Dominici, C., Heitz-Marchaland, C., Zelina, P., Hellal, F., Bradke, F., and Chédotal, A. (2014). A simple method for 3D analysis of immunolabeled axonal tracts in a transparent nervous system. Cell Rep *9*, 1191–1201.

Dufour, A., Seibt, J., Passante, L., Depaepe, V., Ciossek, T., Frisén, J., Kullander, K., Flanagan, J.G., Polleux, F., and Vanderhaeghen, P. (2003). Area specificity and topography of thalamocortical projections are controlled by ephrin/Eph genes. Neuron *39*, 453–465.

Erzurumlu, R.S., and Gaspar, P. (2012). Development and critical period plasticity of the barrel cortex. Eur J Neurosci *35*, 1540–1553.

Erzurumlu, R.S., Murakami, Y., and Rijli, F.M. (2010). Mapping the face in the somatosensory brainstem. Nat Rev Neurosci *11*, 252–263.

Feldheim, D.A., Vanderhaeghen, P., Hansen, M.J., Frisén, J., Lu, Q., Barbacid, M.,

595 and Flanagan, J.G. (1998). Topographic guidance labels in a sensory projection to
596 the forebrain. Neuron *21*, 1303–1313.

597 Fukuchi-Shimogori, T., and Grove, E.A. (2001). Neocortex patterning by the secreted
598 signaling molecule FGF8. Science *294*, 1071–1074.

599 Fukuchi-Shimogori, T., and Grove, E.A. (2003). Emx2 patterns the neocortex by
600 regulating FGF positional signaling. Nat Neurosci *6*, 825–831.

601 Hippenmeyer, S., Vrieseling, E., Sigrist, M., Portmann, T., Laengle, C., Ladle, D.R.,
602 and Arber, S. (2005). A developmental switch in the response of DRG neurons to
603 ETS transcription factor signaling. PLoS Biol *3*, e159.

604 Jen, J.C., Chan, W.-M., Bosley, T.M., Wan, J., Carr, J.R., Rüb, U., Shattuck, D.,
605 Salamon, G., Kudo, L.C., Ou, J., et al. (2004). Mutations in a human ROBO gene
606 disrupt hindbrain axon pathway crossing and morphogenesis. Science *304*, 1509–
607 1513.

608 Kaliszewska, A., Bijata, M., Kaczmarek, L., and Kossut, M. (2012). Experience-
609 dependent plasticity of the barrel cortex in mice observed with 2-DG brain mapping
610 and c-Fos: effects of MMP-9 KO. Cereb Cortex *22*, 2160–2170.

611 Kivrak, B.G., and Erzurumlu, R.S. (2013). Development of the principal nucleus
612 trigeminal lemniscal projections in the mouse. J Comp Neurol *521*, 299–311.

613 Marillat, V., Cases, O., Nguyen Ba Charvet, K.T., Tessier-Lavigne, M., Sotelo, C.,
614 and Chédotal, A. (2002). Spatiotemporal expression patterns of slit and robo genes
615 in the rat brain. J Comp Neurol *442*, 130–155.

616 Melzer, P., Welker, E., Dörfl, J., and Van der Loos, H. (1994). Maturation of the
617 neuronal metabolic response to vibrissa stimulation in the developing whisker-to-
618 barrel pathway of the mouse. Brain Res. Dev. Brain Res. *77*, 227–250.

619 Michalski, N., Babai, N., Renier, N., Perkel, D.J., Chédotal, A., and
620 Schneggenburger, R. (2013). Robo3-driven axon midline crossing conditions
621 functional maturation of a large commissural synapse. Neuron *78*, 855–868.

622 Muckli, L., Naumer, M.J., and Singer, W. (2009). Bilateral visual field maps in a
623 patient with only one hemisphere. Proc Natl Acad Sci USA *106*, 13034–13039.

624 Nahmani, M., and Erisir, A. (2005). VGluT2 immunochemistry identifies
625 thalamocortical terminals in layer 4 of adult and developing visual cortex. J Comp
626 Neurol *484*, 458–473.

627 Nakamura, H., and O'Leary, D.D. (1989). Inaccuracies in initial growth and
628 arborization of chick retinotectal axons followed by course corrections and axon
629 remodeling to develop topographic order. J Neurosci *9*, 3776–3795.

630 Oury, F., Murakami, Y., Renaud, J.-S., Pasqualetti, M., Charnay, P., Ren, S.-Y., and
631 Rijli, F.M. (2006). Hoxa2- and rhombomere-dependent development of the mouse
632 facial somatosensory map. Science *313*, 1408–1413.

633 Penfield, W., and Boldrey, E. (1937). Somatic motor and sensory representation in
634 the cerebral cortex of man as studied by electrical stimulation. Brain *60*, 389–443.

635 Peron, S.P., Freeman, J., Iyer, V., Guo, C., and Svoboda, K. (2015). A Cellular
636 Resolution Map of Barrel Cortex Activity during Tactile Behavior. Neuron *86*, 783–
637 799.

638 Petros, T.J., Rebsam, A., and Mason, C.A. (2008). Retinal axon growth at the optic
639 chiasm: to cross or not to cross. Annu. Rev. Neurosci. *31*, 295–315.

640 Pfeiffenberger, C., Cutforth, T., Woods, G., Yamada, J., Rentería, R.C.,
641 Copenhagen, D.R., Flanagan, J.G., and Feldheim, D.A. (2005). Ephrin-As and neural
642 activity are required for eye-specific patterning during retinogeniculate mapping. Nat
643 Neurosci *8*, 1022–1027.

644 Rash, B.G., and Grove, E.A. (2006). Area and layer patterning in the developing
645 cerebral cortex. Curr Opin Neurobiol *16*, 25–34.

646 Rebsam, A., Petros, T.J., and Mason, C.A. (2009). Switching Retinogeniculate Axon
647 Laterality Leads to Normal Targeting but Abnormal Eye-Specific Segregation That Is
648 Activity Dependent. J Neurosci *29*, 14855–14863.

649 Renier, N., Adams, E.L., Kirst, C., Wu, Z., Azevedo, R., Kohl, J., Autry, A.E., Kadiri,
650 L., Umadevi Venkataraju, K., Zhou, Y., et al. (2016). Mapping of Brain Activity by
651 Automated Volume Analysis of Immediate Early Genes. Cell *165*, 1789–1802.

652 Renier, N., Schonewille, M., Giraudet, F., Badura, A., Tessier-Lavigne, M., Avan, P.,
653 de Zeeuw, C.I., and Chédotal, A. (2010). Genetic dissection of the function of
654 hindbrain axonal commissures. PLoS Biol *8*, e1000325.

655 Renier, N., Wu, Z., Simon, D.J., Yang, J., Ariel, P., and Tessier-Lavigne, M. (2014).
656 iDISCO: a simple, rapid method to immunolabel large tissue samples for volume
657 imaging. Cell *159*, 896–910.

658 Sabatier, C., Plump, A.S., Le Ma, Brose, K., Tamada, A., Murakami, F., Lee, E.Y.-
659 H.P., and Tessier-Lavigne, M. (2004). The divergent Robo family protein rig-1/Robo3
660 is a negative regulator of slit responsiveness required for midline crossing by
661 commissural axons. Cell *117*, 157–169.

662 Sato, M., and Stryker, M.P. (2008). Distinctive features of adult ocular dominance
663 plasticity. J Neurosci *28*, 10278–10286.

664 Simon, D.J., Weimer, R.M., Mclaughlin, T., Kallop, D., Stanger, K., Yang, J., O'leary,
665 D.D.M., Hannoush, R.N., and Tessier-Lavigne, M. (2012). A caspase cascade
666 regulating developmental axon degeneration. J Neurosci *32*, 17540–17553.

667 Staiger, J.F., Bisler, S., Schleicher, A., Gass, P., Stehle, J.H., and Zilles, K. (2000).
668 Exploration of a novel environment leads to the expression of inducible transcription
669 factors in barrel-related columns. Neuroscience *99*, 7–16.

670 Tessier-Lavigne, M. (1995). Eph receptor tyrosine kinases, axon repulsion, and the
671 development of topographic maps. Cell *82*, 345–348.

672 Trevelyan, A.J., Upton, A.L., Cordery, P.M., and Thompson, I.D. (2007). An
673 experimentally induced duplication of retinotopic mapping within the hamster primary
674 visual cortex. Eur J Neurosci *26*, 3277–3290.

675 Voiculescu, O., Charnay, P., and Schneider-Maunoury, S. (2000). Expression pattern
676 of a Krox-20/Cre knock-in allele in the developing hindbrain, bones, and peripheral
677 nervous system. Genesis *26*, 123–126.

678 Waite, P.M., and Cragg, B.G. (1982). The peripheral and central changes resulting
679 from cutting or crushing the afferent nerve supply to the whiskers. Proc. R. Soc.
680 Lond., B, Biol. Sci. *214*, 191–211.

681 Williams, R.W., Hogan, D., and Garraghty, P.E. (1994). Target recognition and visual
682 maps in the thalamus of achiasmatic dogs. Nature *367*, 637–639.

683 Woolsey, T.A., and Van der Loos, H. (1970). The structural organization of layer IV in
684 the somatosensory region (SI) of mouse cerebral cortex. The description of a cortical
685 field composed of discrete cytoarchitectonic units. Brain Res *17*, 205–242.

686

687
688

Figure legends

Figure 1. Rewiring of r3 and r5 derived hindbrain projections to midbrain/forebrain projections in *Robo3$^{R3\text{-}5}$-cKO* mice.
(**A**) Schematic representation of the mouse whisker to barrel somatosensory pathway. (**B**) Top panels: in situ hybridization (*ish*) with a *robo3* probe on coronal sections at rhombomeres 3 and 2 (r3, r2) level in E12 embryos. No staining is observed in *Robo3$^{R3\text{-}5}$-cKO* mice in r3. Trigeminal ganglion (V) neurons do not express *Robo3*. Bottom panels: coronal sections at r3 level in E13 *Robo3$^{R3\text{-}5}$-Het;Tau^{GFP}* or *Robo3$^{R3\text{-}5}$-cKO;Tau^{GFP}* embryos stained for GFP. GFP+ commissures are strongly reduced in mutants, but a few axons are still crossing (arrows)**. (C**) Cytochrome oxidase staining (Cyt. ox.), and ßGal, GFP co-Immunostaining of coronal sections of P4 *Robo3$^{R3\text{-}5}$-Het;Tau^{GFP}* or *Robo3$^{R3\text{-}5}$-cKO;Tau^{GFP}* brains at the level of the brainstem principal trigeminal nucleus (PrV), showing the barrellettes. Rows a to e are indicated. The barrelette patterns and ßGal+ cells distribution is similar in control and *Robo3$^{R3\text{-}5}$-cKO* mutant mice. aVCN: anterior ventral cochlear nucleus. (**D)** flat-mount view and scheme of the hindbrain of E12 *Robo3$^{R3\text{-}5}$-Het;Tau^{GFP}* or *Robo3$^{R3\text{-}5}$-cKO;Tau^{GFP}* embryos. Commissures are strongly reduced at r3 and r5 levels in mutants but a subset of axons still cross in r3 (arrowheads). GFP+ axons still project rostrally towards the midbrain. (**E**) Coronal sections at the level of the forebrain VPM thalamic nucleus and barrel cortex of P0 *controls* or *Robo3$^{R3\text{-}5}$-cKO* brains hybridized with an *ephrin-A5* probe, showing the expression gradients of the molecule, which are unaffected by the conditional deletion of the Robo3.
Scale bars are 400µm, except ish and Cyt. ox (100µm) and **E** (500µm).

Figure 2. Organization of the projections to the VPM
(**A**) Whole-mount immunostaining for GFP in *Robo3$^{R3\text{-}5}$-Het;Tau^{GFP}* and *Robo3$^{R3\text{-}5}$-cKO;Tau^{GFP}* P4 brains cleared with iDISCO. Dorsal projections (left) and lateral projections (right) are shown for each case. The Trigemino Thalamic tract has been color-coded in gray, while the rest of the GFP signal is in green. (**B**) Coronal sections of P4 mouse brain through the sensory thalamus (VPM) stained for cytochrome oxidase. In *Robo3$^{R3\text{-}5}$-Het;Tau^{GFP}* mice, GFP+ axons project to the barreloid area of the VPM. In *Robo3$^{R3\text{-}5}$-cKO;Tau^{GFP}* mice barreloids are found in two regions, a lateral one containing most of the GFP+ axons and a medial one (arrows) containing only a few patches of GFP axons. (**C**) P4 mice injected bilaterally with DiI and DiA at the level of the PrV nucleus. Sections were collected at the level of the VPM. In controls, the PrV-VPM projection is entirely crossed. In mutants, the VPM receives bilateral inputs from the ipsilateral and contralateral PrV. (**D**) P4 hindbrain cross sections at the level of the PrV in controls and mutants after unilateral injections of DiA and DiI in the VPM (depicted in the schematics). In controls, PrV trigemino-thalamic projection neurons are labeled by the dye injected in the contralateral VPM. In mutants, the dorsal PrV also has only contralaterally labeled neurons, whereas the ventral PrV contains interspersed ipsilaterally and contralaterally labeled neurons.
Scale bars are 300µm.

Figure 3. Structure of the VPM maps revealed by ION lesions

Whole-mount scans of 3DISCO cleared P8 *Robo3$^{R3\text{-}5}$-Het;Tau^{GFP}* and *Robo3$^{R3\text{-}5}$-cKO;Tau^{GFP}* brains immunostained for GFP. Optical sections and 3D oblique projections are presented. (**A**) Control and mutant brains, ION intact. The oblique projection reveals the topographic barreloid organization in controls (left panels) or mutants (right panels). In the mutant, the dense and patched domains of GFP+ axons (green and red respectively) were manually segmented. (**B**) Mutant brains, unilateral ION lesions. The data are presented as in **A**. On the side contralateral to the lesion, the barreloids in the patched projection map (red) are fused (n=3), while the topographic organization of the barreloids in the dense GFP+ domain is still visible (green). The opposite is seen on the side ipsilateral to the lesion: the dense domain of GFP+ axons (green) reveals a fused map while rows of barreloids are visible in the patched domain (red). (**C**) Expansion and retraction of the VPM domains in P8 *Robo3$^{R3\text{-}5}$-cKO;Tau^{GFP}* brains after lesions. (**D**) Model of the VPM organization in mutant mice deduced from the lesions experiments.
Scale bars are 300µm.

Figure 4. Bilateral inputs to the VPM in Robo3R3-5-cKO mice
Whole brain iDISCO+ scans from adult mice immunolabeled for c-Fos. The whiskers were shaved on the left side, and B, D rows were spared on the right side. **A** Presentation of the projection plane used in the following panels: a 45° oblique (from both coronal and sagittal) 50µm projection plane was positioned to intersect with the VPM annotation (in red). **B** Details of the c-Fos pattern in the VPM of *Robo3$^{R3\text{-}5}$-Het* and *Robo3$^{R3\text{-}5}$-cKO* mice on each side. In controls, two bands of c-Fos+ cells were seen on the side contralateral to the spared whiskers, revealing the B and D rows barreloids. In *Robo3$^{R3\text{-}5}$-cKO* mice, a dual band pattern in the VPM was seen on both sides of the brain. On the ipsilateral side, the bands were visible on the same intersecting plane as in controls. On the contralateral side, the bands of activity were visible on a plane more medial, at the edge of the VPM annotation. **C** Representation of the VPM organization in the *Robo3$^{R3\text{-}5}$-cKO* mice.
Scale bars are 500µm.

Figure 5. Bilateral inputs to the barrel cortex in Robo3R3-5-cKO mice
(A) tangential sections through the barrel cortex from P10 mice stained for anti-Vglut2. Barrels are more numerous and smaller in mutants. (**B)** Tangential sections through Flat-mounted cortices at the level of the barrel cortex in whisker-deprived adult mice immunostained for Vglut2 and c-Fos. In controls, c-Fos+ cell density is high in the barrel cortex contralateral to the intact whiskers and low on the ipsilateral side. In *Robo3$^{R3\text{-}5}$-cKO* mutants, c-Fos expression is induced bilaterally in complementary domains on either side of the cortex, ipsilateral and contralateral to the stimulated side. (**C**) Interpretation of the results from (**B**). (**D**) Tangential sections through Flat-mounted cortices at the level of the barrel cortex, in whisker-deprived adult mice immunostained for Vglut2 and c-Fos. The left side of the face were fully shaved, while only the first arc (left panels) or b row (right panels) were spared on the right side. Only the contralateral sides are shown for controls. Mutants show bilateral patterns of c-Fos (**E**) Schematic representation of the whisker map deduced from c-Fos activation patterns. (**F**) General model for the wiring of the *Robo3$^{R3\text{-}5}$-cKO* mutant mice.
Scale bars are 200µm.

Figure 6 Activity-dependent competition between ipsilateral and contralateral inputs in mutant barrel cortex

Tangential sections of controls or *Robo3*$^{R3\text{-}5}$*-cKO* flat-mounted P10 cortices stained for cytochrome oxidase in control conditions or after unilateral lesion of the infraorbital nerve (ION) at P1. In *Robo3*$^{R3\text{-}5}$*-Het* controls, the barrels do not form in S1 contralateral to the lesion, whereas a normal map is seen on the ipsilateral side. In *Robo3*$^{R3\text{-}5}$*-cKO* mutants, contralateral to the lesion, barrels form in the domain processing ipsilateral inputs and ipsilateral to the lesion a barreless region is noted in the domain processing ipsilateral inputs. The size of the ipsilateral map is indicated to compare with the maps in unlesioned mutants and controls. Quantification of the surface occupied by the large-whiskers barrels is shown on the right side.
Scale bars are 200µm.

Figure 7 Cortical integration of sensory information
(**A**) ClearMap analysis of the c-Fos patterns in iDISCO+ cleared brains in control and mutant mice after 1h of exploration of a new environment (n=3 for each group). The whiskers were shaved on the left side, and b, d rows were spared on the right side. Heatmaps present averaged c-Fos+ cell densities on both sides for 3 brains for each group, and the p-values maps present the voxels statistically different between the left and right sides, in green when the left side is more active, in red when the right side is more active. At the level of the barrel cortex, as expected the activation was reversed between control and mutant maps in both the VPM and cortex, at the level of the d row (arrowheads). (**B**) iDISCO+ whole-mount c-Fos immunostaining and imaging of adult brains after unilateral stimulation of the rows a, c and e, manually segmented by cortical layers. The pattern in the lower right panel shows the spread of c-Fos+ cells between active rows, but no spill-over of activity from the contralateral map to the adjacent ipsilateral map (arrows show blank rows in layers 2/3).
Scale bars are 400µm.

Figure 1-figure supplement 1

Normal organization of the principal trigeminal nucleus (PrV) in *Robo3$^{R3\text{-}5}$-cKO* mice

(A) Cytochrome oxidase staining of coronal sections of P4 brains at the level of the PrV, showing the barrellettes. Rows a to e are indicated. The barellette pattern is similar in control and *Robo3$^{R3\text{-}5}$-cKO* mutant mice. MV: Trigeminal motor nucleus, d: dorsal PrV, v: ventral PrV. (**B**) Coronal sections at the level of the PrV in adults *Robo3$^{R3\text{-}5}$-Het;Tau^{GFP}*, stained with anti NeuN and anti ßGal. ßGal- and NeuN+ cells can be found in the ventral PrV (arrowheads).
Scale bars, 400µm and 100µm (**A**); 200µm and 50µm (**B**)

Figure 2-figure supplement 1

Tract organization and timing of arrival of Ipsilateral and contralateral projections from the Principal Trigeminal Nucleus (PrV) to the thalamus in the *Robo3$^{R3\text{-}5}$-cKO* embryos.

(A) Coronal sections of E15.5 *Robo3$^{R3\text{-}5}$-cKO ; tau^{GFP}* embryos (n=3) at the rostral-most level where the axon bundle of the trigemino-thalamic tract (TT) is visible, in the developing thalamus. Contralateral projections from the PrV are labeled with DiI, and r3-PrV axons (ipsi and contra) are labeled with GFP. A medio-lateral gradient of DiI+, DiI+/GFP+ and GFP+ axons is seen in the tract, suggesting that contra- and ipsilateral axons are pre-organized in the tract before reaching the thalamus. Moreover, both contralateral and ipsilateral axons are seen at the end of the developing TT, suggesting an absence of a significant delay in the development of the contralateral tract compared to the ipsilateral tract. **(B)** Coronal sections of E18 controls and *Robo3$^{R3\text{-}5}$-cKO ; tau^{GFP}* embryos (n=3) at the level of the VPM, shortly after the arrival of the TT axons from the PrV. In the mutants, GFP+ terminals in both the dense and sparse clusters are visible, suggesting that both ipsi- and contralateral populations of PrV axons are present early in the developing VPM.
Scale bars are 100µm.

Figure 3-figure supplement 1

(A) Detail of the projection plane used to reveal the VPM topography in whole-mount GFP labeled P8 brains cleared with 3DISCO. (**B**) Detail of the manual 3D color-coding used in *Robo3$^{R3\text{-}5}$-cKO;Tau^{GFP}* mutant mice to highlight the different domains of the VPM, based on the pattern of GFP+ terminals (dense or patched). (**C**) Effect of a neonatal lesion of the infraorbital nerve (ION) in controls *Robo3$^{R3\text{-}5}$-Het;Tau^{GFP}* mice. Barreloids are visible on the side ipsilateral to the lesion, but not on the side contralateral where they are indicated as "fused".
Scale bars are 300µm.

Figure 5-figure supplement 1

Tangential sections through cortical layer 4 in adult flat-mounted cortices of control and *Robo3$^{R3\text{-}5}$-cKO* mutant mice stained for Vglut2. Both left and right sides are shown. In mutant animals, the organization of the barrels is similar, but variations on the shape of the inner maps are seen from animal to animal, and also between left and right sides. Scale bars are 500µm.

Figure 5-figure supplement 2

Quantification of the surface of major barrels from tangential sections through cortical layer 4 in P30 control and *Robo3*$^{R3\text{-}5}$*-cKO* mutant mice.

Figure 5-figure supplement 3

(**A**) Tangential sections through cortical layer 4 in P10 flat-mounted cortices of control and *Robo3*$^{R3\text{-}5}$*-cKO* mutant mice stained for cytochrome oxidase (Cyt. ox.). The black dashed outline shows the presence of 2 domains in the mutant map, delimited by a cytochrome oxidase-free band. (**B**) Coronal sections through adult brains at the level of the barrel cortex in whisker-deprived mice immunostained for c-Fos and Hoechst. Barrels in layer 4 are indicated. In controls, c-Fos+ cell density is high in the barrel cortex contralateral to the intact whiskers and low on the ipsilateral side. In *Robo3*$^{R3\text{-}5}$*-cKO* mutants, c-Fos expression is induced bilaterally in complementary domains on either side of the cortex, ipsilateral and contralateral to the stimulated side. Of note, the bilateral activation of c-Fos in mutants is visible across all cortical layers.
Scale bars are 200µm.

Figure 7-figure supplement 1

ClearMap analysis of the c-Fos patterns in iDISCO+ cleared brains in control and mutant mice after 1h of exploration of a new environment (n=3 for each group). Projections of the dorsal cortex are shown. The mice whiskers were shaved on the left side, and B, D rows were spared on the right side. Heatmaps present averaged c-Fos+ cell densities on both sides for 3 brains for each group, and the p-values maps present the voxels statistically different between the left and right sides, in green when the left side is more active, in red when the right side is more active.
Scale bars are 2mm.

Video 1. Rhombomere 3 projections from the brainstem to the VPM

Whole-mount immunostaining for GFP in *Robo3*$^{R3\text{-}5}$*-Het;Tau*^{GFP} P4 brains cleared with 3DISCO. The GFP is showed in green, and the trigemino-thalamic tract has been color-coded in gray.

Video 2. Segmentation of the VPM in *Robo3*$^{R3\text{-}5}$*-Het;Tau*^{GFP} mutants

Whole-mount immunostaining for GFP in *Robo3*$^{R3\text{-}5}$*-Het;Tau*^{GFP} P8 brains cleared with 3DISCO. The GFP dense cluster is segmented in green, and the GFP+ patches are color-coded in red.

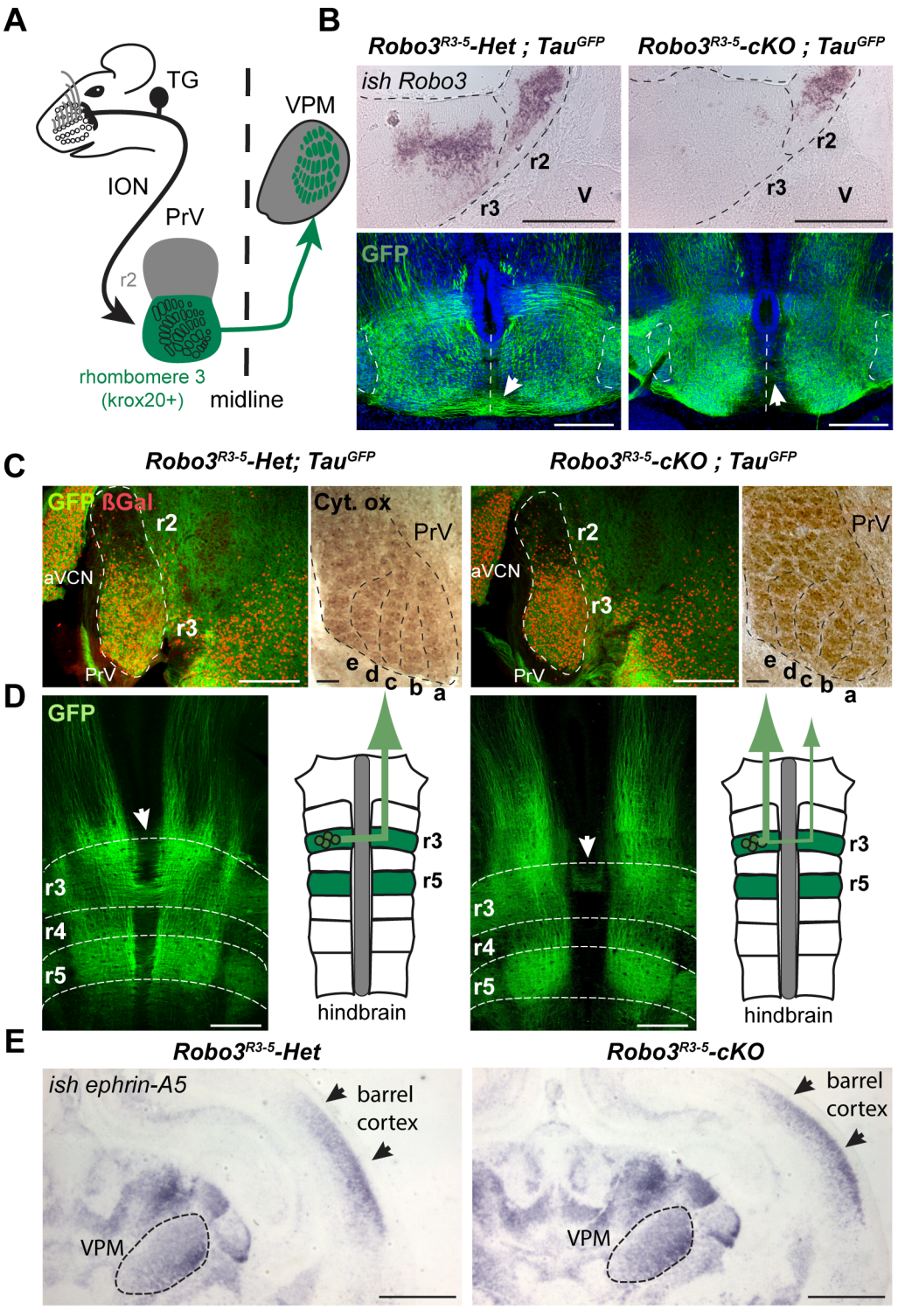
A
TG
VPM
ION
PrV
r2
rhombomere 3
(krox20+)
midline
B
Robo3R3-5-Het ; TauGFP
Robo3R3-5-cKO ; TauGFP
ish Robo3
r2
r3
V
GFP
C
Robo3R3-5-Het; TauGFP
Robo3R3-5-cKO ; TauGFP
GFP ßGal
aVCN
Cyt. ox
PrV
e d c b a
D
GFP
r3
r4
r5
hindbrain
E
Robo3R3-5-Het
Robo3R3-5-cKO
ish ephrin-A5
barrel
cortex
VPM

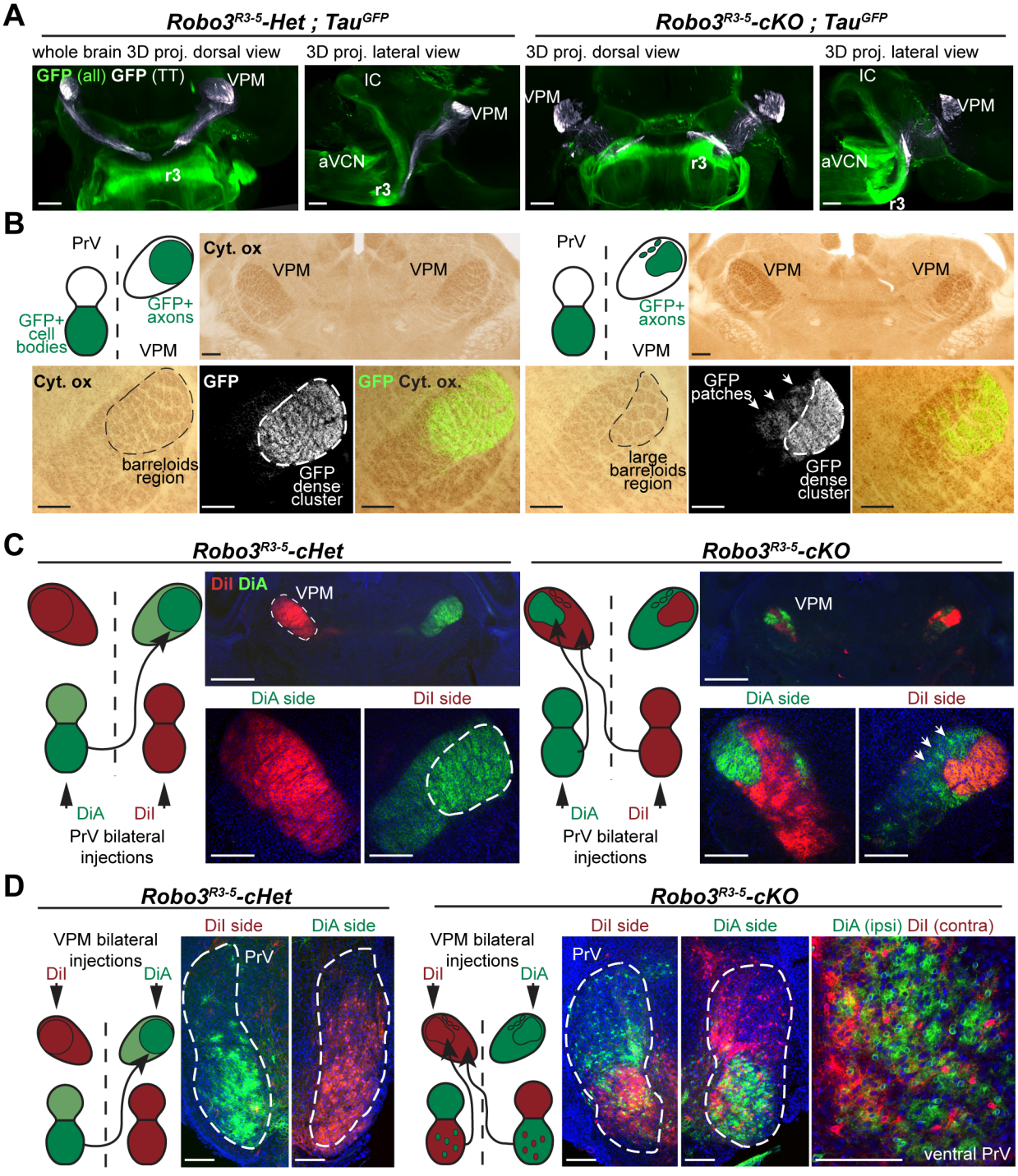
A
Robo3R3-5-Het ; TauGFP
Robo3R3-5-cKO ; TauGFP
whole brain 3D proj. dorsal view
3D proj. lateral view
3D proj. dorsal view
3D proj. lateral view
GFP (all) GFP (TT)
VPM
IC
aVCN
r3
B
PrV
GFP+ cell bodies
GFP+ axons
VPM
Cyt. ox
barreloids region
GFP
GFP dense cluster
GFP Cyt. ox.
large barreloids region
GFP patches
C
Robo3R3-5-cHet
Robo3R3-5-cKO
DiI DiA
DiA side
DiI side
DiA
DiI
PrV bilateral injections
D
Robo3R3-5-cHet
Robo3R3-5-cKO
VPM bilateral injections
DiI side
DiA side
DiA (ipsi) DiI (contra)
PrV
ventral PrV

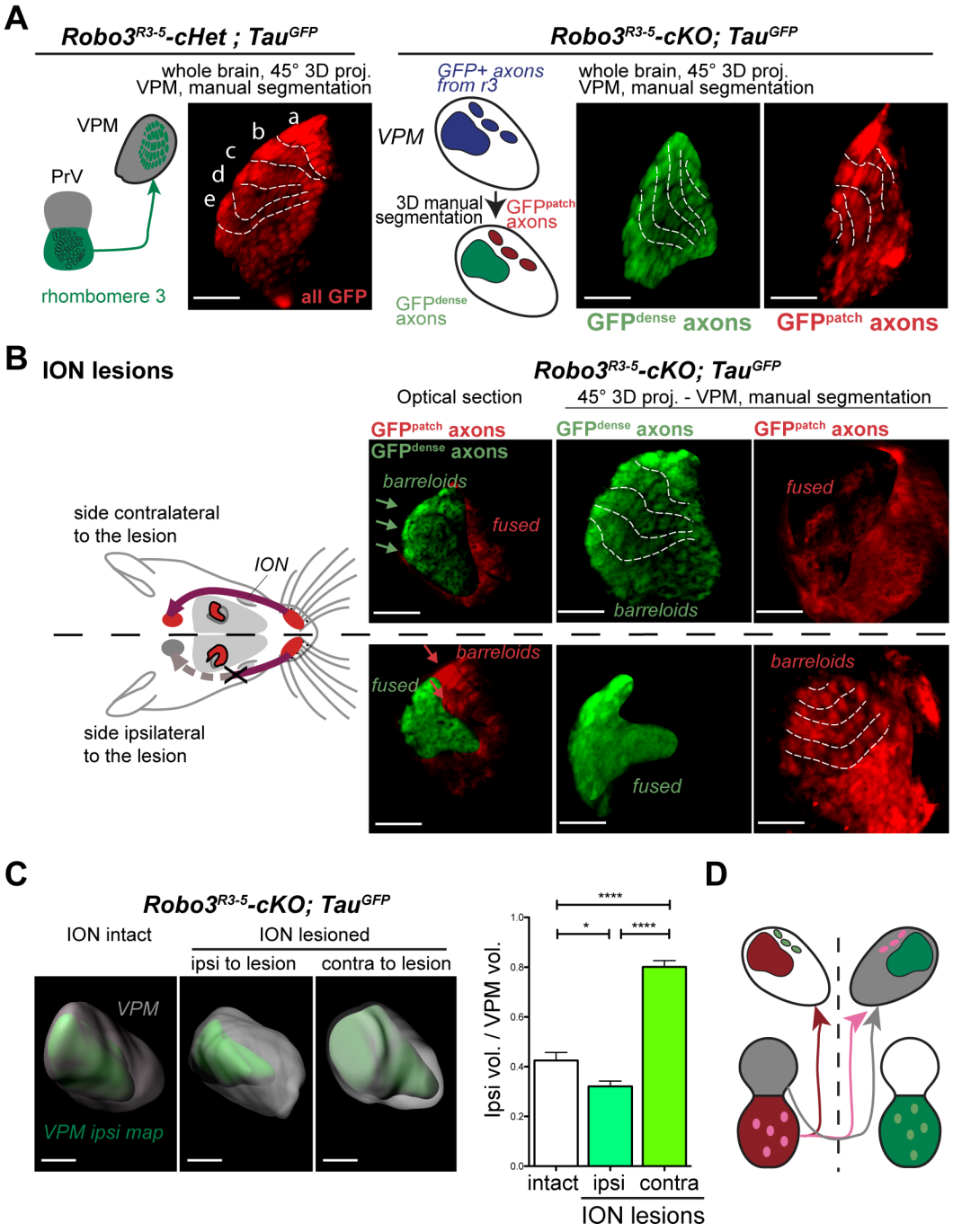
A
Robo3R3-5-cHet ; TauGFP
whole brain, 45° 3D proj.
VPM, manual segmentation
VPM
PrV
rhombomere 3
a
b
c
d
e
all GFP
Robo3R3-5-cKO; TauGFP
GFP+ axons
from r3
VPM
3D manual
segmentation
GFPpatch
axons
GFPdense
axons
whole brain, 45° 3D proj.
VPM, manual segmentation
GFPdense axons
GFPpatch axons
B
ION lesions
Robo3R3-5-cKO; TauGFP
Optical section
45° 3D proj. - VPM, manual segmentation
GFPpatch axons
GFPdense axons
GFPpatch axons
side contralateral
to the lesion
ION
barreloids
fused
barreloids
fused
side ipsilateral
to the lesion
barreloids
fused
fused
barreloids
C
Robo3R3-5-cKO; TauGFP
ION intact
ION lesioned
ipsi to lesion
contra to lesion
VPM
VPM ipsi map
****
*
****
Ipsi vol. / VPM vol.
1.0
0.8
0.6
0.4
0.2
0.0
intact
ipsi
contra
ION lesions
D

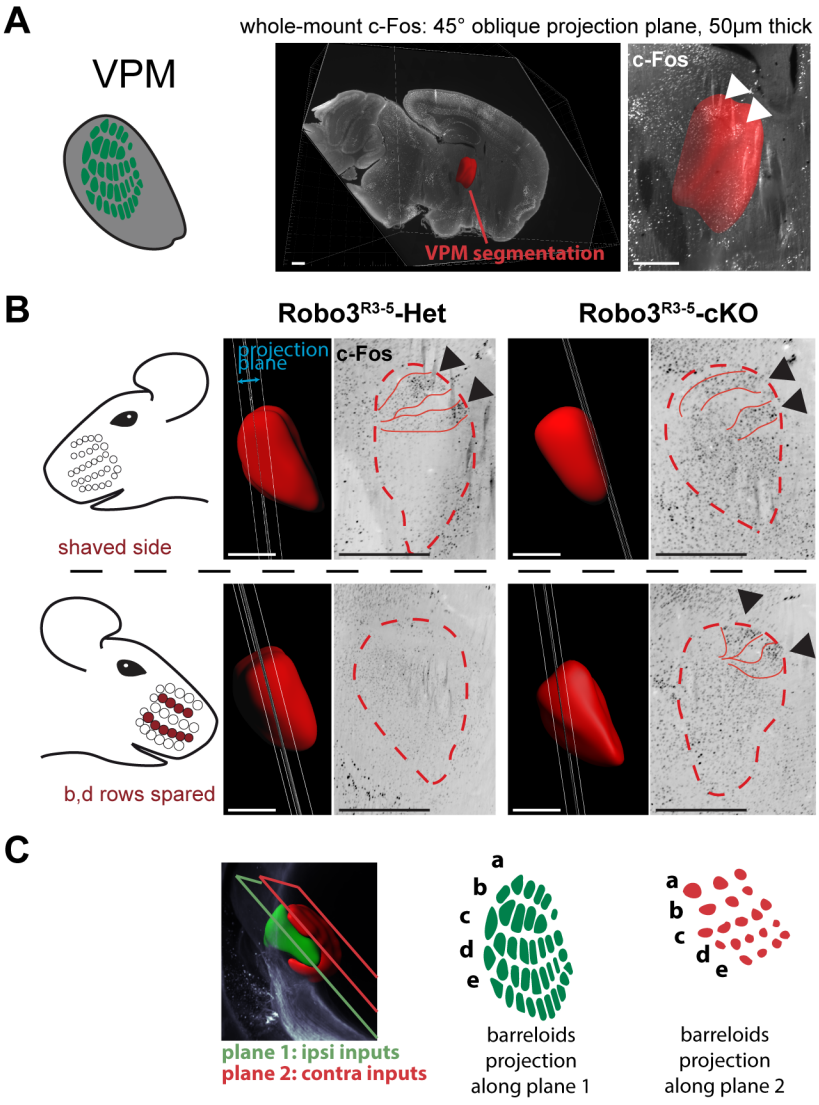
A
whole-mount c-Fos: 45° oblique projection plane, 50µm thick
VPM
VPM segmentation
c-Fos
B
Robo3R3-5-Het
Robo3R3-5-cKO
projection plane
c-Fos
shaved side
b,d rows spared
C
plane 1: ipsi inputs
plane 2: contra inputs
a
b
c
d
e
barreloids projection along plane 1
barreloids projection along plane 2

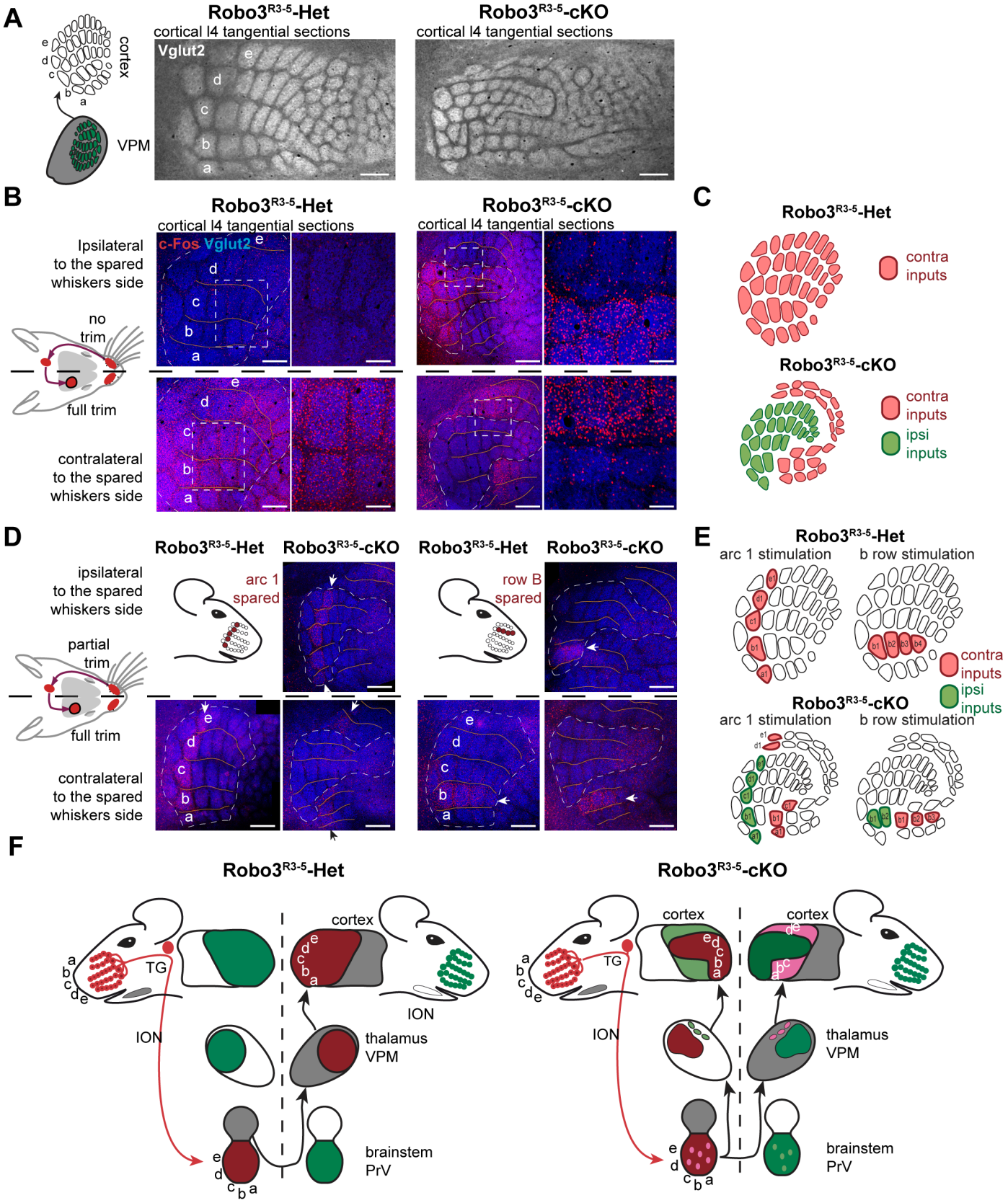
A
Robo3R3-5-Het
cortical l4 tangential sections
Robo3R3-5-cKO
cortical l4 tangential sections
Vglut2
cortex
VPM
B
Robo3R3-5-Het
cortical l4 tangential sections
Robo3R3-5-cKO
cortical l4 tangential sections
c-Fos Vglut2
Ipsilateral to the spared whiskers side
no trim
full trim
contralateral to the spared whiskers side
C
Robo3R3-5-Het
contra inputs
Robo3R3-5-cKO
contra inputs
ipsi inputs
D
Robo3R3-5-Het
Robo3R3-5-cKO
Robo3R3-5-Het
Robo3R3-5-cKO
arc 1 spared
row B spared
ipsilateral to the spared whiskers side
partial trim
full trim
contralateral to the spared whiskers side
E
Robo3R3-5-Het
arc 1 stimulation
b row stimulation
contra inputs
ipsi inputs
Robo3R3-5-cKO
arc 1 stimulation
b row stimulation
F
Robo3R3-5-Het
Robo3R3-5-cKO
TG
ION
cortex
thalamus VPM
brainstem PrV

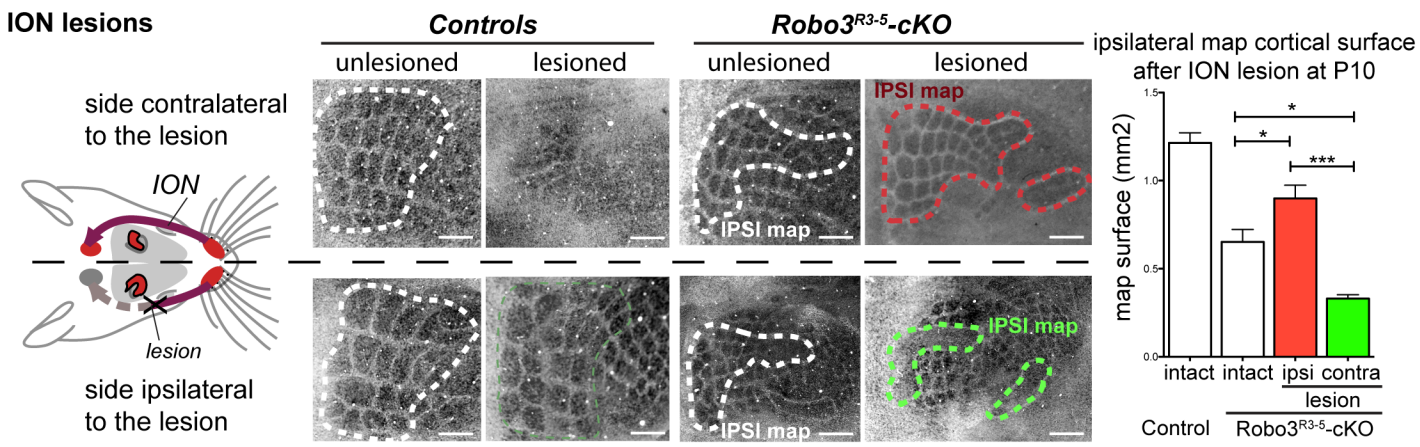
ION lesions
Controls
Robo3R3-5-cKO
unlesioned
lesioned
unlesioned
lesioned
side contralateral
to the lesion
ION
lesion
side ipsilateral
to the lesion
IPSI map
IPSI map
IPSI map
IPSI map
ipsilateral map cortical surface
after ION lesion at P10
map surface (mm2)
1.5
1.0
0.5
0.0
*
*
***
intact
intact
ipsi
contra
lesion
Control
Robo3R3-5-cKO

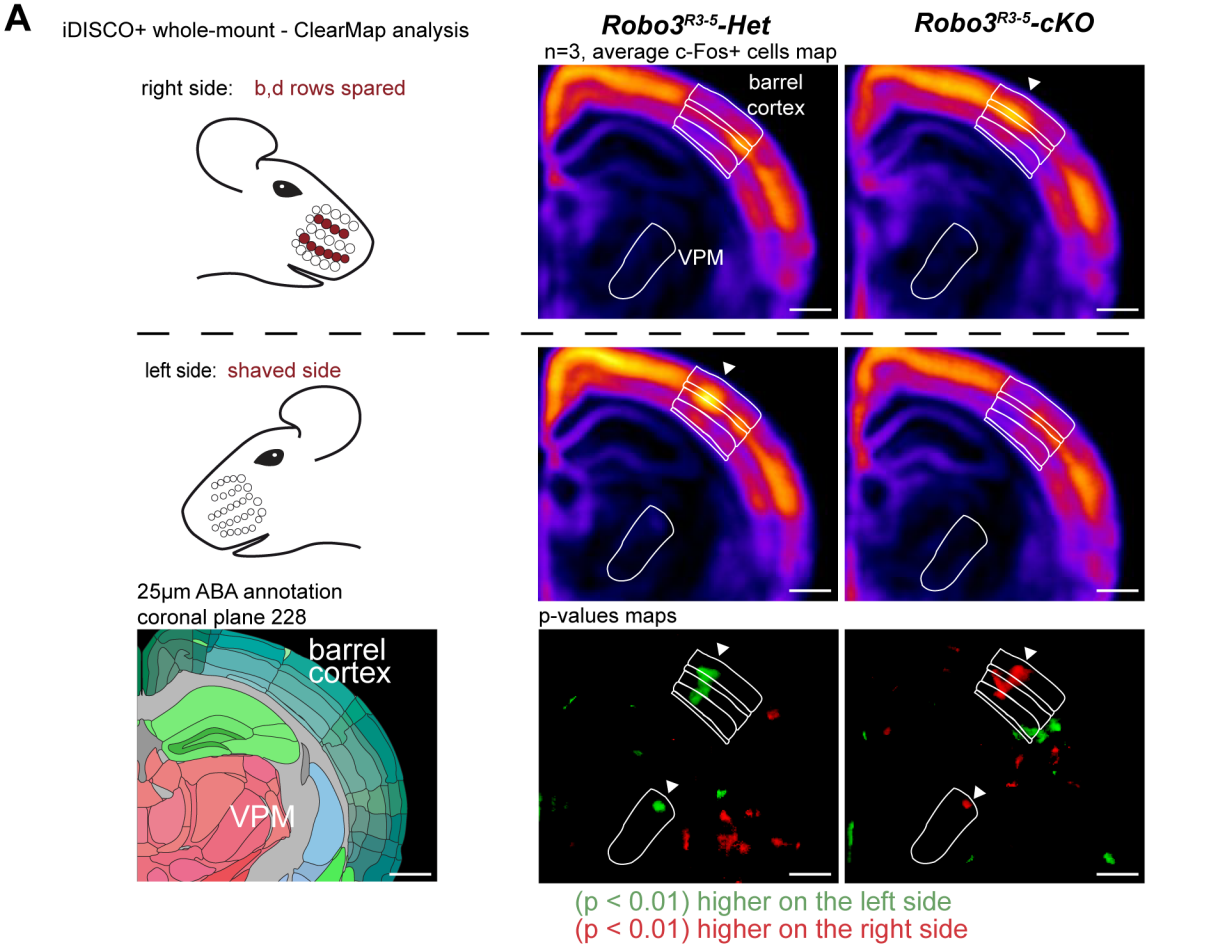
A
iDISCO+ whole-mount - ClearMap analysis
Robo3R3-5-Het
Robo3R3-5-cKO
n=3, average c-Fos+ cells map
right side: b,d rows spared
barrel cortex
VPM
left side: shaved side
25µm ABA annotation
coronal plane 228
barrel cortex
VPM
p-values maps
(p < 0.01) higher on the left side
(p < 0.01) higher on the right side

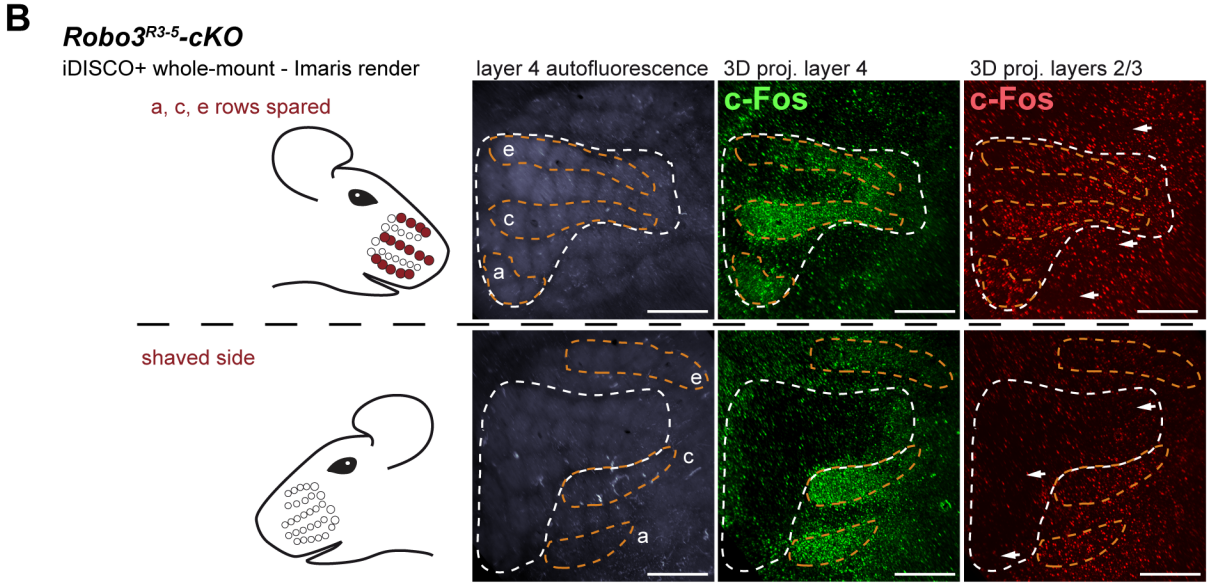
B
Robo3R3-5-cKO
iDISCO+ whole-mount - Imaris render
a, c, e rows spared
layer 4 autofluorescence
3D proj. layer 4
3D proj. layers 2/3
c-Fos
c-Fos
shaved side
e
c
a

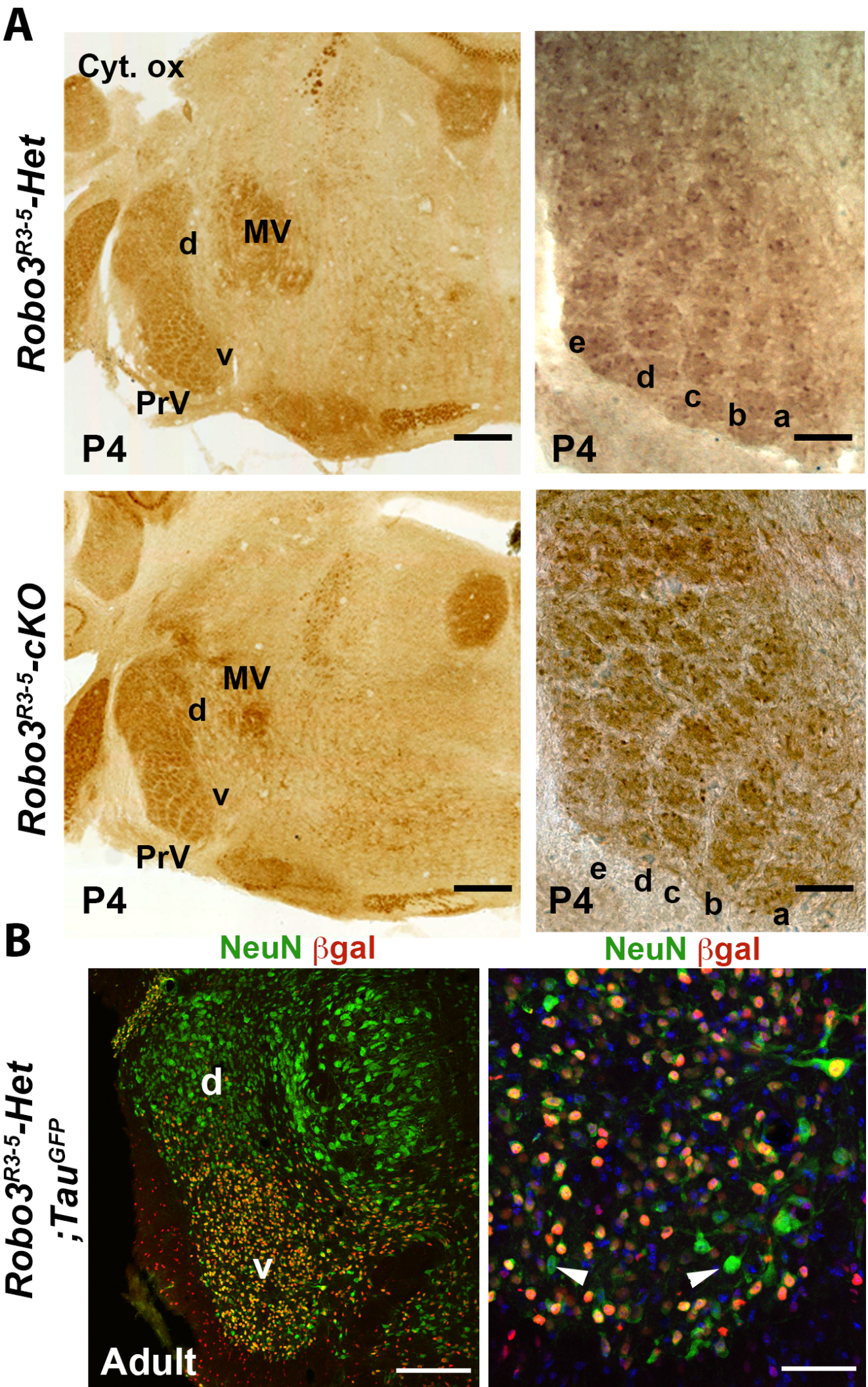
A
Robo3R3-5-Het
Cyt. ox
d
MV
v
PrV
P4
e
d
c
b
a
P4
Robo3R3-5-cKO
MV
d
v
PrV
P4
e
d
c
b
a
P4
B
NeuN βgal
NeuN βgal
Robo3R3-5-Het
;TauGFP
d
v
Adult

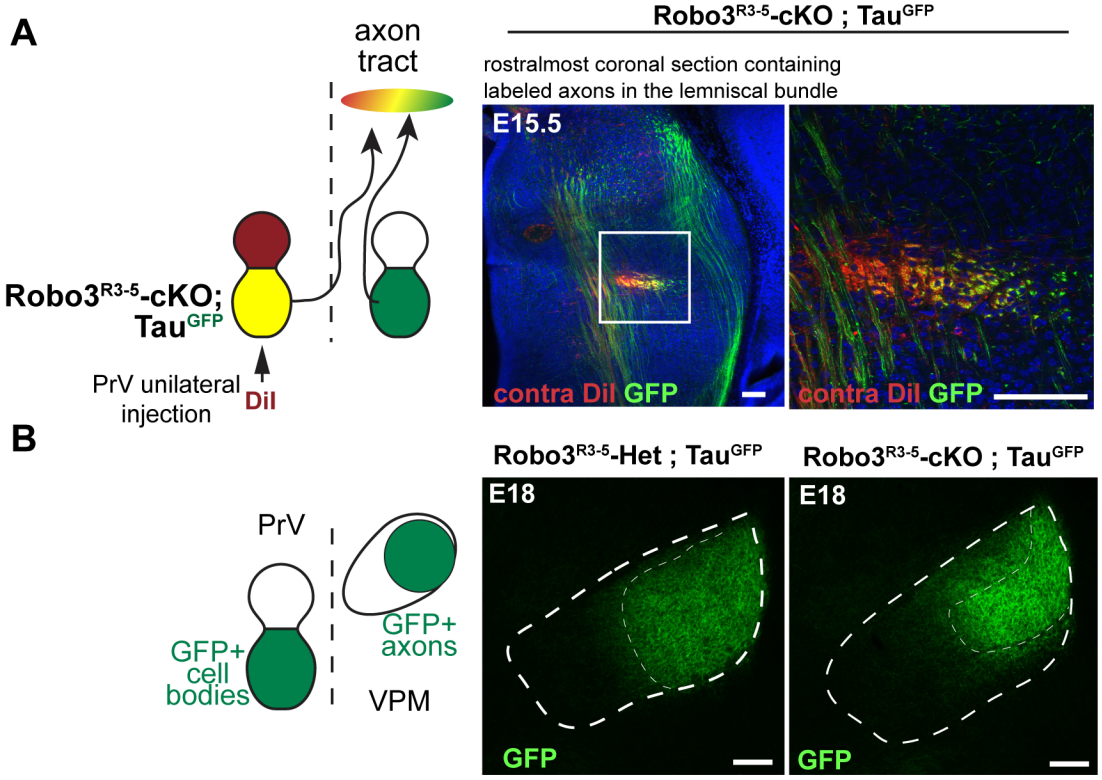
A
axon tract
Robo3R3-5-cKO; TauGFP
PrV unilateral injection
DiI
Robo3R3-5-cKO ; TauGFP
rostralmost coronal section containing labeled axons in the lemniscal bundle
E15.5
contra DiI GFP
contra DiI GFP
B
PrV
GFP+ cell bodies
GFP+ axons
VPM
Robo3R3-5-Het ; TauGFP
Robo3R3-5-cKO ; TauGFP
E18
E18
GFP
GFP

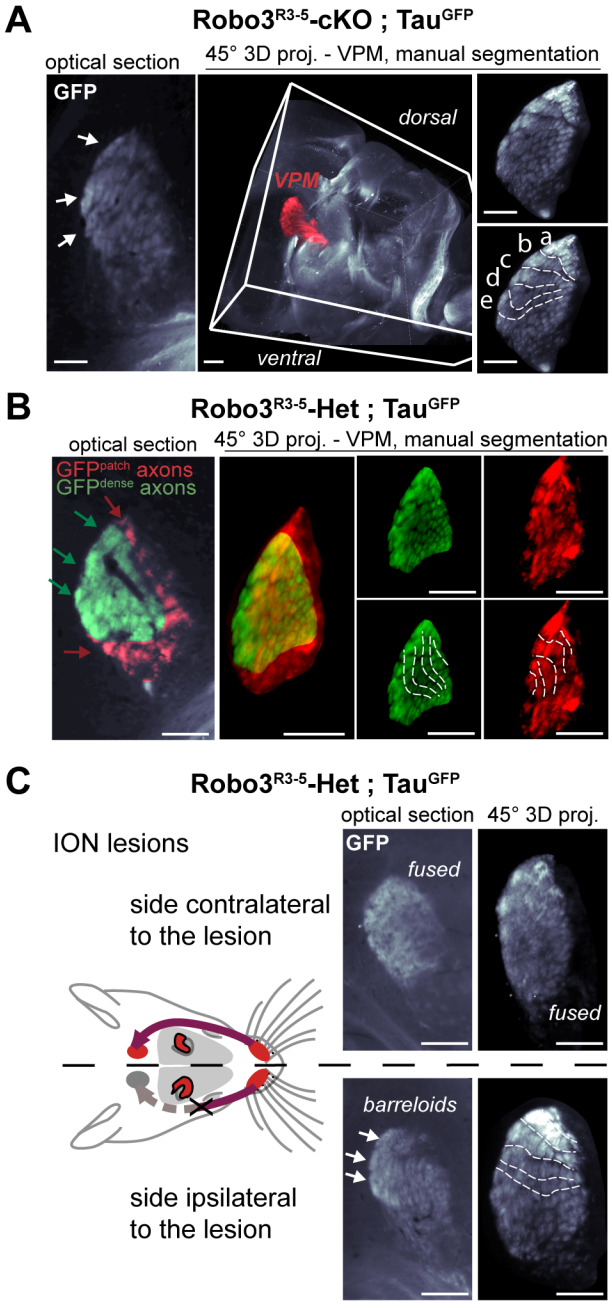
A
Robo3R3-5-cKO ; TauGFP
optical section
45° 3D proj. - VPM, manual segmentation
GFP
dorsal
VPM
ventral
a
b
c
d
e
B
Robo3R3-5-Het ; TauGFP
optical section
45° 3D proj. - VPM, manual segmentation
GFPpatch axons
GFPdense axons
C
Robo3R3-5-Het ; TauGFP
ION lesions
optical section
45° 3D proj.
GFP
fused
fused
side contralateral
to the lesion
barreloids
side ipsilateral
to the lesion

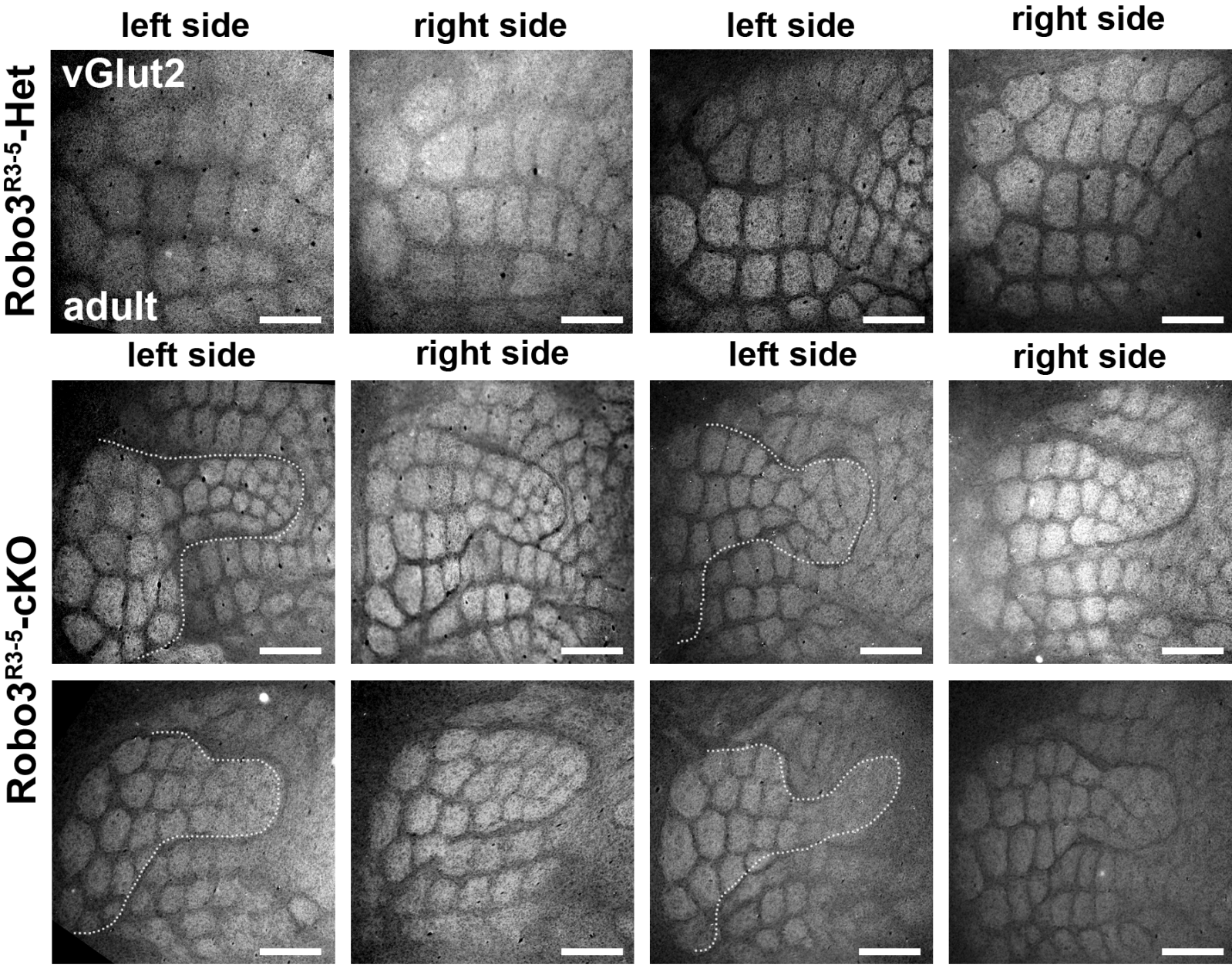
left side
right side
left side
right side
vGlut2
adult
Robo3R3-5-Het
left side
right side
left side
right side
Robo3R3-5-cKO

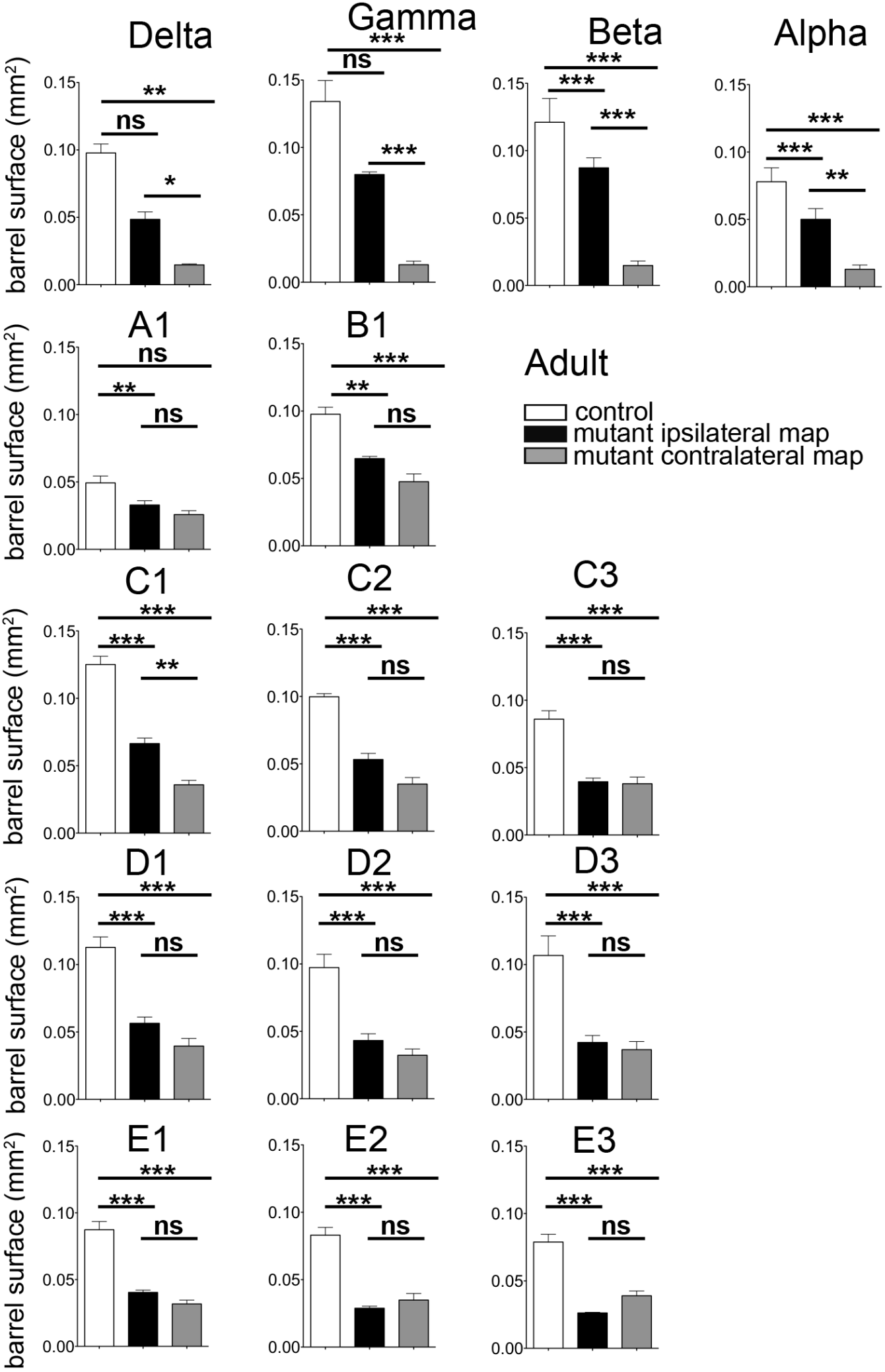
Delta
Gamma
Beta
Alpha
A1
B1
Adult
control
mutant ipsilateral map
mutant contralateral map
C1
C2
C3
D1
D2
D3
E1
E2
E3
barrel surface (mm²)
0.15
0.10
0.05
0.00
ns
*
**
***

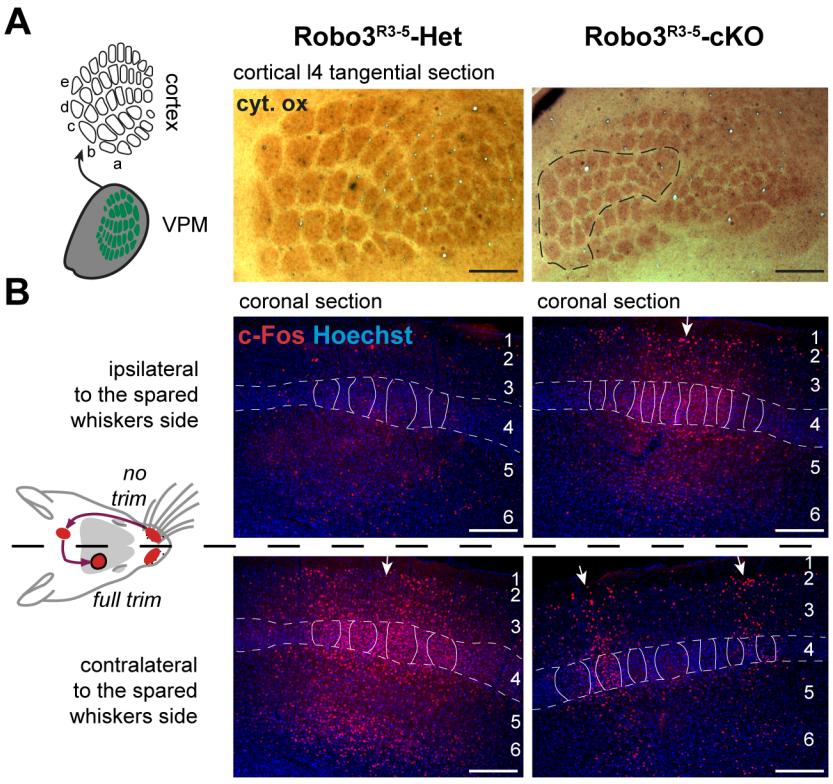
A
Robo3R3-5-Het
Robo3R3-5-cKO
cortical l4 tangential section
cyt. ox
e
d
c
b
a
cortex
VPM
B
coronal section
coronal section
c-Fos Hoechst
ipsilateral
to the spared
whiskers side
no
trim
full trim
contralateral
to the spared
whiskers side
1
2
3
4
5
6

cortical projection, 25µm ABA annotation

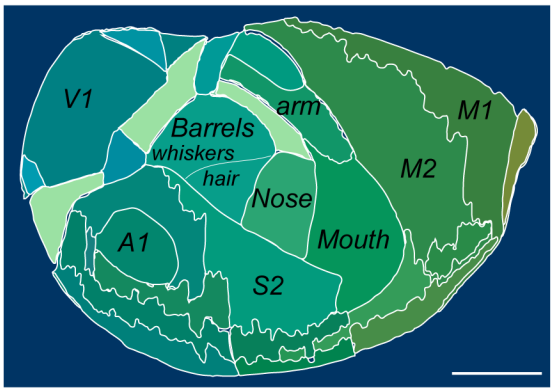

Robo3^{R3-5}-Het **Robo3^{R3-5}-cKO**

n=3, average c-Fos+ cells map

right side:
b,d rows spared

left side:
shaved side

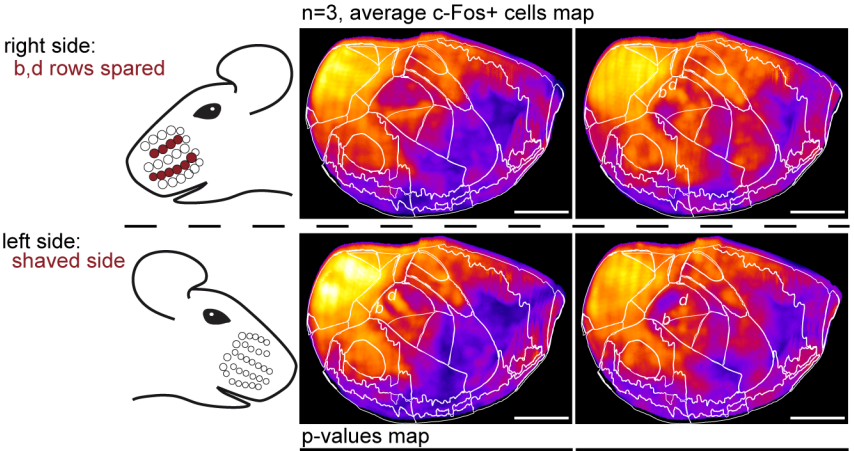

p-values map

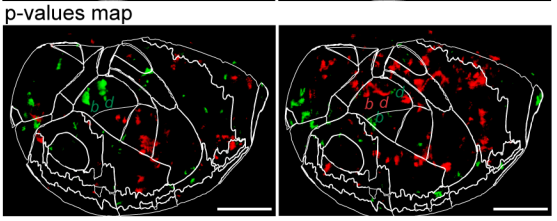

(p < 0.01) higher on the left side
(p < 0.01) higher on the right side